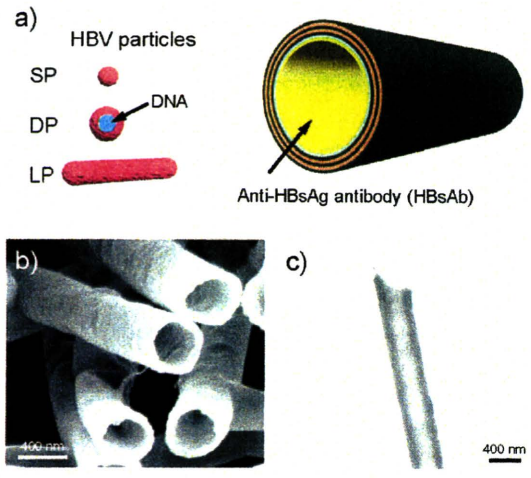

Figure 1. (a) Schematic illustrations of three types of HBV particles (SP, DP, LP) and $(PLA/HSA)_2PLA/PLG/HBsAb$ nanotube (AbNT). (b) SEM image of lyophilized AbNTs prepared using porous PC template (D_p = 400 nm), and (c) TEM image of AbNT stained with uranylacetate.

The amount of HBsAb on the pore surface was estimated. The powder of AbNTs (*ca.* 210 μg) obtained from one PC membrane (diameter, 25 mm), in which *ca.* 3.0×10^8 channels exist, was dispersed in acidic water (pH 3.5, 1.5 mL) to dissolve the multilayered structure. From the absorbance at 280 nm, the HBsAb concentration was determined to be *ca.* 75 nM, under the assumption that the AbNTs consist of the LbL assembly described above. It became apparent that one AbNT (length, 9 μm) contains *ca.* 2.2×10^5 molecules of HBsAb.

We used three different HBV solutions (HBV1−3) for trap experiments: HBsAg SP solution (HBV1), HBsAg-positive plasma including all particles (SP, DP, and LP) (HBV2), and DP-rich solution (HBV3). Actually, SP, DP, and LP can all be detected by HBsAg assay; only DP is found by DNA assay. First, HBV1 (1 μg/mL, 7.5 μL) was added to the AbNT dispersion (pH 7.4, 0.75 mL) in phosphate buffered saline (PBS). To avoid an electrostatic attraction between the HBV particles and tube surface exterior, free HSA was added to the nanotube dispersion ([HSA] = 0.2 mM). After incubation for 3 h at room temperature, the mixture was centrifuged for 10 min at 5000 × *g* to spin down the tubes. The HBV-trapping capability of the AbNT was determined using chemiluminescence enzyme immunoassay (CLEIA) of the remaining HBsAg in the supernatant. The amount of HBsAg was significantly lower than that of the identically treated HBV1 solution without the tubes (control group) (Figure 2a). The trapping ratio [{1 − COI(AbNT)/COI-(Control)} × 100] reached 90%. In contrast, incubation with the $(PLA/HSA)_3PLA$ nanotubes (NTs) did not cause a marked difference in the HBsAg numbers. Chemiluminescence immunoassay (CLIA) yielded similar results (Figure S1). Remarkably, CLEIA and CLIA measurements were not reproducible for the PBS solution without 0.2 mM HSA. In SDS PAGE of the concentrated supernatant, no HBsAb band appeared between 130 and 150 kDa. This manifests that the AbNTs retain their original multilayered structure without the antibody release during the experiments. We concluded that the HBV SPs diffused into the hollow space of the AbNT and bind to the inner surface wall. The concentration dependence of the absorbed HBsAg (Figure S2)

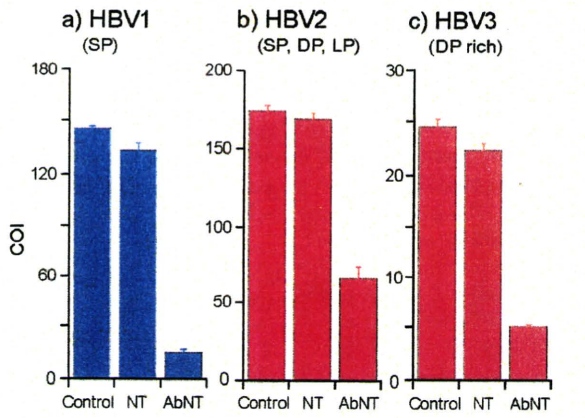

Figure 2. Amount of remaining HBsAg in HBV1−3 solutions (PBS, pH 7.4, 0.2 mM HSA) after incubation with AbNTs, with NTs, and without tubes (control) determined using the CLEIA method. The vertical axis is defined as the cutoff index (COI).

Table 1. Amount of Remaining DNA in HBV2 and HBV3 Solutions (PBS, pH 7.4, 0.2 mM HSA) after Incubation with AbNTs

[DNA] (copies/mL)	HBV2	HBV3
Control (without tubes)	1.23×10^5	2.58×10^5
AbNT	166	36
Trapping ratio (%)	99.87	99.99

conferred a binding constant (K) of 3.5×10^7 M^{-1}. Generally, the K value of the antigen−antibody reaction is between 10^8 and 10^9 M^{-1}. The low binding affinity of HBsAg (SP) to the AbNT appears to be attributable to the fact that some HBsAbs are adhered to the pore wall with unfavorable geometries, in which the antigen-binding fragments do not direct to the hollow center.

Next, we performed the same experiments using more practical HBV2 and HBV3 solutions. After incubation with the AbNTs for 3 h, the mixture was centrifuged to precipitate the tubes. The CLEIA of the supernatants demonstrated that the HBsAg-trapping ratio was, respectively, 62% for HBV2 and 79% for HBV3 (Figure 2b, c); these values are lower than that observed in the case of HBV1. At least two plausible reasons exist. First, HBV2 and HBV3 include certain amounts of LPs that are too large to enter the pore (*ca.* 200 nm). Second, a nonspecific antibody reaction takes place, because HBV2 and HBV3 are prepared from the HBsAg-positive plasma. The soluble inhibitor is likely to contribute the reduction of trap competence.

To evaluate the DP-trapping capability of the AbNT, DNA quantification assays of the supernatants were conducted by PCR. As presented in Figure 2b and 2c (control groups), the amount of HBsAg in the HBV3 solution was one-seventh of that of the HBV2 solution. Strikingly however, the DNA concentration in HBV3 (2.58×10^5 copies/mL) was 2-fold greater than that of HBV2 (Table 1). Therefore, HBV3 contains large quantities of infectious DPs. To our surprise, the DNA concentrations declined dramatically after incubation with the AbNTs: 166 copies/mL for HBV2 (trapping ratio, 99.87%) and 36 copies/mL for HBV3 (trapping ratio, 99.99%). We reasoned that DPs were entirely captured into the one-dimensional pore space of the AbNT, although noninfectious SPs and LPs still

dx.doi.org/10.1021/ja1096122 |J. Am. Chem. Soc. 2011, 133, 3246–3248

existed in the bulk solution. TEM observation demonstrated the entrapping of DPs into the hollow (Figure S3). Results show that the AbNT treated HBV specimens became clinically DP free. The detailed supramolecular mechanism responsible for this perfect DP trapping into the AbNT remains unclear. Nevertheless, we presume that (i) dense and robust DP with genome DNA is favorable to bind to the pore wall of the cylinder or (ii) the large DP can possess multiple binding sites per particle that might enhance encapsulation.

In conclusion, the virus trap set in the blood protein nanotube ensnared the infectious HBV Dane particles selectively and completely. The efficiency of removal by a single AbNT treatment reached −3.9 *log* order. This astonishing result will serve as a trigger to engender a new field of virus detecting and removing devices. For instance, elimination of small and nonenvelope type viruses, such as hepatitis E virus and human parvo B19 virus, using HSA nanotubes would be of tremendous medical importance. Recombinant HSA is currently manufactured on an industrial scale,[16] which enables us to exploit the protein nanotubes in practical use.

■ ASSOCIATED CONTENT

Supporting Information. Experimental section, amount of remaining HBsAg in HBV1 solution after incubation with AbNTs determined using CLIA method (Figure S1), concentration dependence of absorbed HBsAg (HBV1) in AbNTs (Figure S2), and TEM of AbNT incorporating DPs (Figure S3). This material is available free of charge via the Internet at http://pubs.acs.org.

■ AUTHOR INFORMATION

Corresponding Author
komatsu@kc.chuo-u.ac.jp

■ ACKNOWLEDGMENT

This work was supported by a Grant-in-Aid for Scientific Research on Innovative Area "Coordination Programming" (Area 2107, No. 21108013) from MEXT Japan, a Grant-in-Aid for Scientific Research (B) (No. 20350058) from JSPS, PRESTO "Control of Structure and Functions" JST, and Health Science Research Grants from MHLW. Skillful experiments on the synthesis of protein nanotubes conducted by Ms. Nao Kobayashi are gratefully acknowledged.

■ REFERENCES

(1) (a) Shimizu, T.; Masuda, M.; Minamikawa, H. *Chem. Rev.* **2005**, *105*, 1401–1443. (b) Yui, H.; Shimidzu, Y.; Kamiya, S.; Yamashita, I.; Masuda, M.; Ito, K.; Shimizu, T. *Chem. Lett.* **2005**, *34*, 232–233. (c) Kameta, N.; Masuda, M.; Minamikawa, H.; Mishima, Y.; Yamashita, I.; Shimizu, T. *Chem. Mater.* **2007**, *19*, 3553–3560.

(2) (a) Graveland-Bikker, J. F.; Ipsen, R.; Otte, J.; de Kruif, C. G. *Langmuir* **2004**, *20*, 6841–6846. (b) Graveland-Bikker, J. F.; Schaap, I. A. T.; Schmidt, C. F.; de Kruif, C. G. *Nano Lett.* **2006**, *6*, 616–621.

(3) Geng, Y.; Dalhaimer, P.; Cai, S.; Tsai, R.; Tewari, M.; Minko, T.; Discher, D. E. *Nat. Nanotechnol.* **2007**, *2*, 249–255.

(4) (a) Mitchell, D. T.; Lee, S. B.; Trofin, L.; Li, N.; Nevanen, T. K.; Söderlund, H.; Martin, C. R. *J. Am. Chem. Soc.* **2002**, *124*, 11864–11865. (b) Hou, S.; Wang, J.; Martin, C. R. *Nano Lett.* **2005**, *5*, 231–234. (c) Hillebrenner, H.; Buyukserin, F.; Stewart, J. D.; Martin, C. R. *J. Nanosci. Nanotechnol.* **2007**, *7*, 2211–2221.

(5) Son, S. J.; Reichel, J.; He, B.; Schuchman, M.; Lee, S. B. *J. Am. Chem. Soc.* **2005**, *127*, 7316–7317.

(6) (a) Liang, Z.; Sucha, A. S.; Yu, A.; Caruso, F. *Adv. Mater.* **2003**, *15*, 1849–1853. (b) Yu, A.; Liang, Z.; Caruso, F. *Chem. Mater.* **2005**, *17*, 171–175. (c) Wang, Y.; Angelatos, A. S.; Caruso, F. *Chem. Mater.* **2008**, *20*, 848–858.

(7) (a) Ai, S.; Lu, G.; He, Q.; Li, J. *J. Am. Chem. Soc.* **2003**, *125*, 11140–11141. (b) He, Q.; Cui, Y.; Ai, S.; Tian, Y.; Li, J. *Curr. Opin. Colloid Interface Sci.* **2009**, *14*, 115–125.

(8) Lee, D.; Cohen, R. E.; Rubner, M. F. *Langmuir* **2007**, *23*, 123–129.

(9) Qu, X.; Komatsu, T. *ACS Nano* **2010**, *4*, 563–573.

(10) (a) Kim, D. H.; Karan, P.; Göring, P.; Leclaire, J.; Caminade, A.-M.; Majoral, J.-P.; Gösele, U.; Steinhart, M.; Knoll, W. *Small* **2005**, *1*, 99–102. (b) Steinhart, M. *Adv. Polym. Sci.* **2008**, *220*, 123–187.

(11) Lok, A. S. F.; McMahon, B. J. *Hepatology* **2001**, *34*, 1225–1241.

(12) Bertoletti, A.; Gehring, A. J. *J. Gen. Virol.* **2006**, *87*, 1439–1449.

(13) Maya, R.; Gershwin, M. E.; Shoenfeld, Y. *Clinic Rev. Allerg. Immunol.* **2008**, *34*, 85–102.

(14) Knipe, D. M.; Howley, P. M.; Griffin, D. E.; Lamb, R. A.; Martin, M. A.; Roizman, B.; Straus, S. E. *Fields Virology*; Lippincott Williams & Wilkins: Philadelphia, 2007.

(15) (a) Kato, N.; Caruso, F. *J. Phys. Chem. B* **2005**, *109*, 19604–19612. (b) Cortez, C.; Tomaskovic-Crook, E.; Johnston, A. P. R.; Scott, A. M.; Nice, E. C.; Heath, J. K.; Caruso, F. *ACS Nano* **2007**, *1*, 93–102.

(16) Kobayashi, K. *Biologicals* **2006**, *34*, 55–59.

Special Issue: Short Communication Article

Polymers Advanced Technologies

Received: 9 November 2010, Revised: 3 December 2010, Accepted: 20 December 2010, Published online in Wiley Online Library: 2011

(wileyonlinelibrary.com) DOI: 10.1002/pat.1921

Protein nanotubes bearing a magnetite surface exterior†

Teruyuki Komatsu[a]* and Nao Kobayashi[b]

This communication describes the synthesis and structure of multilayered protein nanotubes bearing a magnetite (Fe_3O_4) surface exterior, and their binding capability for zinc(II)-protoporphyrin IX (ZnPP) in aqueous medium. The nanotubes were fabricated using an alternating layer-by-layer (LbL) assembly of human serum albumin (HSA) and poly-L-arginine (PLA) in a track-etched polycarbonate (PC) membrane (pore size, 400 nm), which had been precoated in advance with Fe_3O_4 nanoparticles. Dissolution of the PC template yielded Fe_3O_4(PLA/HSA)$_3$ nanotubes. SEM measurements revealed the formation of uniform hollow cylinders with 417 ± 16 nm outer diameter and 56 ± 7 nm wall thickness. TEM observations confirmed the homogeneous outer surface of Fe_3O_4. In an aqueous medium, the nanotubes captured ZnPP into the swollen wall. The ZnPP-loaded protein nanotubes were collected by exposure to a magnetic field. Copyright © 2011 John Wiley & Sons, Ltd.

Keywords: human serum albumin; layer-by-layer assembly; magnetite; nanotubes; protein

INTRODUCTION

Magnetic-field assisted bioseparation using spherical nanoparticles including a magnetite (Fe_3O_4) component has attracted considerable interest because of its potential applications in various medical fields.[1–5] Colloidal particles, however, confront structural limitations when multi-functionalities must be introduced on the surface. The nanocylindrical hollow structure presents several advantages over spherical particles. The nanotubes can possess different interior and exterior surfaces independently. Therefore it is possible to program desired functions into the pore space, tubular wall, and outer surface of the cylinder. Furthermore, the open-end terminals enable quick loading and release of the target molecule without structural change. Nevertheless, few reports describe the use of magnetic nanotubes for bioseparation in an aqueous medium.[6–8] Lee and co-workers demonstrated that magnetic silica nanotubes are useful for drug delivery.[6] Rubner and co-workers synthesized heterostructured magnetic nanotubes made of layer-by-layer (LbL) assembly of poly(allylamine hydrochloride) and poly(styrene sulfonate), and characterized their molecular transport properties.[7] Li's group developed LbL magnetic nanotubes comprising poly(amino acid)s as a DNA carrier.[8] We recently presented an efficient method to prepare protein nanotubes through alternating LbL assembly in a porous PC membrane.[9] Subsequent dissolution of the template in *N,N*-dimethylformamide (DMF) and freeze-drying of the extracted core yields uniform hollow cylinders as lyophilized powder. The tubes typically comprise six layers of negatively charged human serum albumin (HSA) and positively charged poly-L-arginine (PLA) [(PLA/HSA)$_3$]. The HSA is the major protein of blood plasma; it serves as a transporter of hydrophobic endogenous and exogenous compounds.[10,11] The HSA components in the (PLA/HSA)$_3$ nanotubes retain their original ligand binding ability in water. Therefore the tube walls capture cyanine dye, zinc(II)-protoporphyrin IX (ZnPP), and fatty acids, which are all ligands for HSA.[9] A protein nanotube bearing a ferrimagnetic layer would enable synthesis of magnetically responsive cylinders for protein-based biomolecular separation, transport, and analysis. This paper reports, for the first time, the synthesis and structure of HSA nanotubes bearing an Fe_3O_4 surface exterior and their ZnPP-capturing capability in a biological medium. The ZnPP-loaded nanotubes can be removed easily using a magnetic field.

EXPERIMENTAL

Materials and apparatus

Poly-L-arginine hydrochloride (PLA, Mw: *ca.* 70,000), human serum albumin (HSA, recombinant product expressed by yeast species *Pichia pastoris*), and zinc(II)-protoporphyrin IX (ZnPP) were purchased from Sigma-Aldrich Corp. The Fe_3O_4 nanoparticles [EMG607, 100 mg/ml, particle (*ca.* 10 nm) is covered with cationic surfactant] were purchased from Ferrotec Corp., Japan. The water was deionized (18.2 MΩcm) using water purification systems (Elix UV and Simpli Lab-UV; Millipore Corp.). The fluorescence emission spectra were measured using a spectrofluorometer (FP-6500; Jasco Corp.).

Template synthesis of protein nanotubes with Fe_3O_4 surface exterior

Magnetic protein nanotubes were prepared according to our previously reported procedure with some modifications.[9] The

* *Correspondence to: T. Komatsu, Department of Applied Chemistry, Faculty of Science and Engineering, Chuo University, 1-13-27 Kasuga, Bunkyo-ku, Tokyo 113-8551, Japan.*
E-mail: komatsu@kc.chuo-u.ac.jp

a *T. Komatsu*
Department of Applied Chemistry, Faculty of Science and Engineering, Chuo University, 1-13-27 Kasuga, Bunkyo-ku, Tokyo 113-8551, Japan

b *N. Kobayashi*
Research Institute for Science and Engineering, Waseda University, 3-4-1 Okubo, Shinjuku-ku, Tokyo 169-8555, Japan

† *This work is dedicated to Dr Eishun Tsuchida, Professor Emeritus, Waseda University, Japan.*

Copyright © 2011 John Wiley & Sons, Ltd.

track-etched polycarbonate (PC) porous membrane (Isopore membrane, $r = 25$ mm, pore diameter (D_p) = 400 nm; Millipore Corp.) was placed into a stainless steel syringe holder (25 mm; Advantec Mfg., Inc.) and the aqueous Fe_3O_4 nanoparticle solution (1 mg/ml, 10 ml) was filtered (0.25 ml/min) three times using a syringe pump (PHD-2000; Harvard Apparatus). Then the membrane was removed from the holder and rinsed with deionized water and wiped gently on both sides using a cotton swab to eliminate adherent Fe_3O_4. The obtained pale-brownish membrane was dried in an automatic low-humidity chamber (Super Dry; Tokyo Living Co. Ltd., Japan) for 12 hr (humidity < 1%) and set again into the holder. The sodium phosphate buffered (PB) solution (pH 7.0, 10 mM, 10 ml) of PLA (1 mg/ml) containing 0.1 M NaCl was injected slowly into the pores (0.25 ml/min) to absorb the positively charged PLA. After washing excess PLA using water filtration, the membrane was dried *in vacuo* for 10 min. Next, the PB solution (pH 7.0, 10 mM, 10 ml) of HSA (2 mg/ml) was filtered (0.5 ml/min) through the membrane. Loosely adsorbed proteins were washed with water. Then the membrane was dried under vacuum. These pressure infiltrations were repeated for three cycles to grow the LbL thin film of a combination of PLA/HSA. The PC membrane surface was wiped using a cotton swab and dried in an automatic low-humidity chamber. To eliminate the nanotube cores from the template, the membrane was immersed into a DMF solution and the released cores were freeze-dried *in vacuo*, yielding the Fe_3O_4(PLA/HSA)$_3$ nanotubes as a dark-yellow powder.

SEM and TEM observations

SEM measurements of the magnetic protein nanotubes were conducted as described elsewhere.[9] For TEM observations, 3 μL of the aqueous solution of the Fe_3O_4(PLA/HSA)$_3$ nanotubes was placed onto an elastic carbon-coated copper grid (100 mesh; Okenshoji Co. Ltd.), which was hydrophilized using a hydrophobic treatment device (HDT-400; JEOL Datum). These specimens were observed directly without staining using a transmission electron microscope (JEM-1011; JEOL) with accelerating voltage of 100 kV.

ZnPP binding to Fe_3O_4(PLA/HSA)$_3$ nanotubes

The lyophilized powder of the Fe_3O_4(PLA/HSA)$_3$ nanotubes (*ca.* 60 μg) was dispersed in the PB solution (pH 7.0, 10 mM, 15% DMSO, 1.5 ml). The mixture was sonicated briefly and transferred to a 10-mm path length optical quartz cuvette. The ZnPP (25 μM in DMSO, 12 μL) was added to the nanotube dispersion and the mixture ([ZnPP] = 0.2 μM) was incubated for 3 hr at room temperature in the dark. Then the dispersion was transferred to a glass tube and centrifuged for 10 min at 4000 × *g* to spin off the nanotubes. The fluorescence of the supernatant was measured to assay the concentration of the unbound free ZnPP in the solution. An identically treated control sample without nanotubes was always prepared; its fluorescence intensity was regarded as a 100% ZnPP concentration. The ZnPP-loaded nanotubes can be removed more quickly by exposure to a magnetic field using a Neodymium magnet (468 mT, 5 mm ϕ × 10 mm). The supernatant was transferred carefully to the other quartz cuvette and its fluorescence of the solution was measured to assay the concentration of the unbound ZnPP.

RESULTS AND DISCUSSION

The magnetic protein nanotubes were prepared using an alternating LbL deposition technique with a track-etched PC membrane. First, the PC template (pore diameter, D_p = 400 nm) was placed in the stainless syringe holder and the Fe_3O_4 nanoparticle solution (1 mg/ml, 10 ml) was filtered three times using a syringe pump. The resultant membrane was removed from the holder and rinsed with deionized water. After drying for 12 hr, the pale-brownish PC template was again set in the holder and three-cycle injections of the PLA solution, followed by the HSA solution, were performed according to our previously reported procedure.[9] This sequential LbL build-up assembly of the combination of PLA and HSA produced Fe_3O_4(PLA/HSA)$_3$ multilayers on the pore walls. Careful dissolution of the PC template in DMF and freeze-drying of the extracted core yielded a dark-yellow powder. The SEM observations revealed the formation of highly ordered arrays of the Fe_3O_4(PLA/HSA)$_3$ nanotubes with outer diameter of 417 ± 16 nm (Fig. 1A and 1B). The maximum length of the tubules (*ca.* 9 μm) corresponded to the PC membrane pore depth. The wall thickness was 56 ± 7 nm, which is slightly thicker than that observed in the (PLA/HSA)$_3$ nanotubes (50 ± 4 nm).[9] We proposed a seven-layered cylinder model based on the general principle of LbL membrane growth (Fig. 1C). First the Fe_3O_4 nanoparticles adhered on the negatively charged pore of the PC template, forming the Fe_3O_4 thin films as the first layer. Then the positively charged PLA deposited on the Fe_3O_4 coated surface. Next, the negatively charged HSA was deposited on the PLA layer to produce a new anionic surface. The average thickness of a PLA/HSA bilayer in the (PLA/HSA)$_3$ nanotubes was 16.7 nm.[9] Applying this dimension to the Fe_3O_4(PLA/HSA)$_3$ nanotubes, the outer surface layer of Fe_3O_4 was estimated as *ca.* 6 nm.

TEM observations of the Fe_3O_4(PLA/HSA)$_3$ nanotubes without staining yielded positive images (Fig. 1D). Remarkably, the cylinders

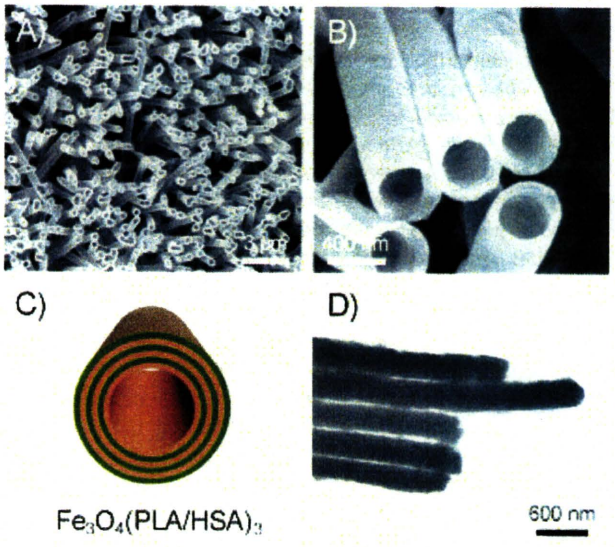

Figure 1. (A, B) SEM images of Fe_3O_4(PLA/HSA)$_3$ nanotubes prepared using porous PC template (D_p = 400 nm), (C) schematic illustration of seven-layered nanotubes with an Fe_3O_4 surface exterior, and (D) TEM image of Fe_3O_4(PLA/HSA)$_3$ nanotubes without staining. This figure is available in color online at wileyonlinelibrary.com/journal/pat

Copyright © 2011 John Wiley & Sons, Ltd.

were totally dark, which suggests that the protein nanotube was wrapped homogeneously in the magnetic Fe_3O_4 thin layer.

Hemin [iron(III)-protoporphyrin IX, FePP] released from methemoglobin is captured by HSA in the human circulatory system, by which it is transported to the liver. Crystallographic studies of the HSA–FePP complex revealed that the FePP was bound in a D-shaped hydrophobic cavity in subdomain IB of HSA.[12] The central iron(III) atom is coordinated by phenolate oxygen of tyrosine-161. We found that zinc(II)-protoporphyrin IX (ZnPP) was also incorporated into the identical site of HSA with a binding constant of $4.4 \times 10^5\ M^{-1}$,[9] and that the HSA–ZnPP complex acts as a photosensitizer for H_2 generation from water.[13] The lyophilized $Fe_3O_4(PLA/HSA)_3$ nanotubes were suspended in sodium phosphate buffered (PB) solution (50 mM, pH 7.0, 15% DMSO, 1.5 ml) and the ZnPP was added to the dispersion ([ZnPP] = 0.2 μM). The fluorescence of ZnPP in the nanotubes could not be evaluated aculately, because the tube dispersion was slightly turbid. After 3 hr in the dark at room temperature, the mixture was centrifuged for 10 min at $4000 \times g$ to remove the nanotubes. Several micrometer cylinders are sufficiently long to spin off by centrifugation. The fluorescence intensity of the supernatant was markedly lower (15%) than that of the identically treated ZnPP solution without the tubes (Fig. 2). Fluorescence of the ZnPP solution incubated with $(PLA/PLG)_3$ nanotubes, which were prepared with poly-L-glutamic acid (PLA) instead of HSA, remained 82% of the control value.[9] Based on these results, it can be concluded that ZnPP can diffuse into the swollen wall of the $Fe_3O_4(PLA/HSA)_3$ nanotubes and that it is bound to the HSA components in the wall. The ratio of the ZnPP/HSA was estimated as *ca.* 0.7 mol/mol. The ZnPP capturing capability of the $Fe_3O_4(PLA/HSA)_3$ nanotubes was fundamentally identical to that of the $(PLA/HSA)_3$ nanotubes in terms of their general features,[9] meaning that

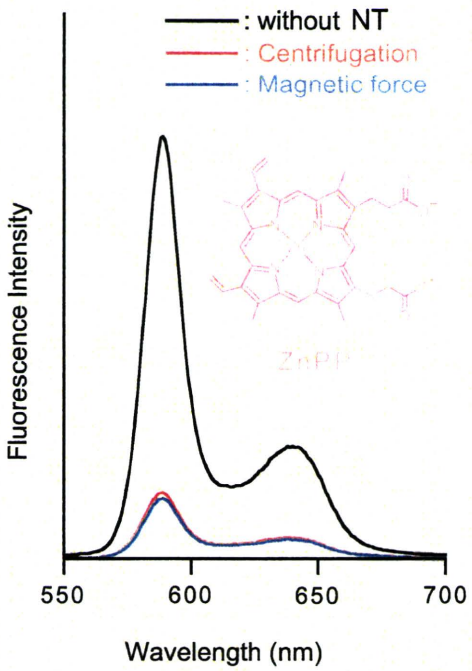

Figure 2. Fluorescence spectra of PB solution (pH 7.0, 10 mM, 15% DMSO) of ZnPP (0.2 μM) after incubation with $Fe_3O_4(PLA/HSA)_3$ nanotubes, with subsequent removal of the ZnPP-loaded nanotubes by centrifugation or magnetic force. This figure is available in color online at wileyonlinelibrary.com/journal/pat

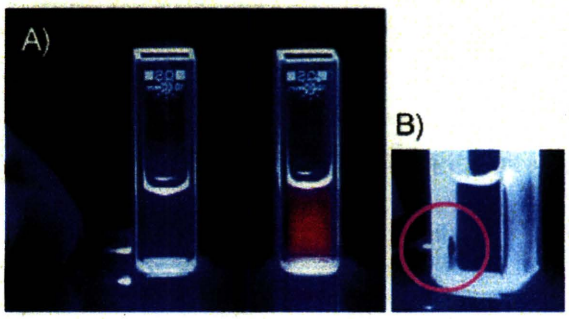

Figure 3. (A) Photographs of PB solution (pH 7.0, 10 mM, 15% DMSO) of ZnPP (0.2 μM) before adding $Fe_3O_4(PLA/HSA)_3$ nanotubes (right) and after incubation with $Fe_3O_4(PLA/HSA)_3$ nanotubes, with subsequent collection of the tubes using a magnetic field (left). (B) Photograph of ZnPP-loaded nanotubes collected on the cuvette wall using a small magnet. This figure is available in color online at wileyonlinelibrary.com/journal/pat

the introduction of the magnetic Fe_3O_4 surface exterior does not disturb the molecular capturing ability of the HSA layer in the walls.

As expected, the ZnPP-loaded $Fe_3O_4(PLA/HSA)_3$ nanotubes can be removed easily by exposure to a magnetic field. By bringing a Neodymium magnet close to the quartz cuvette including the ZnPP solution with the $Fe_3O_4(PLA/HSA)_3$ nanotubes, the pink tubules were attracted rapidly to the magnet; the solution became almost colorless (Fig. 3). The fluorescence intensity of the supernatant was identical to that of the centrifuged sample: 14% intensity of the control (Fig. 2). Detaching the magnet from the cuvette liberated the nanotubes in the solution immediately. This magnetic-field induced collection–dispersion was observed to be reversible. The results explained herein imply that the introduction of the magnetic surface exterior onto the HSA nanotubes excludes the tedious centrifugation process to separate the ligand-bound nanotubes from the bulk solution.

CONCLUSION

We have shown template synthesis of protein nanotubes bearing an Fe_3O_4 surface exterior and characterized their ZnPP-binding capability. In fact, ZnPP can diffuse into the multilayered walls of the cylinders and is captured by HSA components. The ZnPP-bound nanotubes were collected and liberated reversibly using a small magnet, which suggests that simply depositing Fe_3O_4 nanoparticles at the first layer of the protein nanotubes would enable us to create various molecular separation and transport devices that can be controlled magnetically in practical applications.

Acknowledgements

This work was supported by a Grant-in-Aid for Scientific Research on Innovative Area "Coordination Programming" (Area 2107, No. 21108013) from MEXT Japan, a Grant-in-Aid for Scientific Research (B) (No. 20350058) from JSPS, PRESTO "Control of Structure and Functions" JST, and Health Science Research Grants from MHLW.

REFERENCES

[1] S. Sun, H. Zeng, *J. Am. Chem. Soc.* **2002**, *124*, 8204–8205.
[2] C. Xu, S. Sun, *Polym. Int.* **2007**, *56*, 821–826.
[3] A. Ito, M. Shinkai, H. Honda, T. Kobayashi, *J. Biosci. Bioeng.* **2005**, *1*, 1–11.

Copyright © 2011 John Wiley & Sons, Ltd.

[4] M. Namdeo, S. Saxena, R. Tankhiwale, M. Bajpai, Y. M. Mohan, S. K. Bajpai, *J. Nanosci. Nanotech.* **2008**, *8*, 3247–3271.
[5] A. H. Latham, M. E. Williams, *Acc. Chem. Res.* **2008**, *41*, 411–420.
[6] S. J. Son, J. Reichel, B. He, M. Schuchman, S. B. Lee, *J. Am. Chem. Soc.* **2005**, *127*, 7316–7317.
[7] D. Lee, R. E. Cohen, M. F. Rubner, *Langmuir* **2007**, *23*, 123–129.
[8] Q. He, Y. Tian, Y. Cui, H. Mohwald, J. Li, *J. Mater. Chem.* **2008**, *18*, 748–754.
[9] X. Qu, T. Komatsu, *ACS Nano* **2010**, *4*, 563–573.
[10] T. Peters, *All about Albumin: Biochemistry, Genetics and Medical Applications*, Academic Press, San Diego, **1996**.
[11] U. Kragh-Hansen, *Dan. Med. Bull.* **1990**, *37*, 57–84.
[12] P. A. Zunszain, J. Guhman, T. Komatsu, E. Tsuchida, S. Curry, *BMC Strct. Biol.* **2003**, *3*, 6.
[13] T. Komatsu, R-M. Wang, E. Tsuchida, P. A. Zunszain, S. Curry, *J. Am. Chem. Soc.* **2006**, *128*, 16297–16301.

View this article online at wileyonlinelibrary.com Copyright © 2011 John Wiley & Sons, Ltd.

BRAIN RESEARCH 1320 (2010) 69–73

available at www.sciencedirect.com

ScienceDirect

www.elsevier.com/locate/brainres

BRAIN RESEARCH

Research Report

RBC velocities in single capillaries of mouse and rat brains are the same, despite 10-fold difference in body size

Miyuki Unekawa[a], *Minoru Tomita*[a], *Yutaka Tomita*[a], *Haruki Toriumi*[a], *Koichi Miyaki*[b,1], *Norihiro Suzuki*[a,*]

[a]*Department of Neurology, School of Medicine, Keio University, 35 Shinanomachi, Shinjuku-ku, Tokyo 160-8582, Japan*
[b]*Department of Preventive Medicine for Cerebrovascular Disease, School of Medicine, Keio University, 35 Shinanomachi, Shinjuku-ku, Tokyo 160-8582, Japan*

ARTICLE INFO

Article history:
Accepted 12 January 2010
Available online 18 January 2010

Keywords:
Frequency distribution function
Microcirculation
Mouse
RBC velocity
Cerebral cortex

ABSTRACT

Employing high-speed camera laser-scanning confocal microscopy with RBC-tracking software, we previously showed that RBC velocities in intraparenchymal capillaries of rat cerebral cortex are distributed over a wide range. In the present work, we measured RBC velocities in mice, whose body weights are less than one-tenth of that of rats. In an isoflurane-anesthetized mouse, a cranial window was opened in the left temporo-parietal region. Intravenously administered FITC-labeled RBCs were automatically recognized and tracked frame-by-frame at 500 fps, and the velocities of all RBCs recognized were calculated with our Matlab-domain software, KEIO-IS2. Among 15241 RBCs detected in the ROI in 21 mice, 1655 were identified as flowing in capillaries. The velocities of these RBCs ranged from 0.15 to 8.6 mm/s, with a mean of 2.03±1.42 mm/s. A frequency distribution plot showed that RBC velocities were clustered at around 1.0 mm/s, tailing up to 8.6 mm/s, and 59% of the RBCs in capillaries showed velocities within the range of 0.5 to 2.0 mm/s. Unexpectedly, these characteristics of RBC velocities in mice were very similar to those of rats, despite differences in RBC diameter (6.0 vs. 6.5 μm), body size (25 vs. 327 g), heart rate (461 vs. 319 bpm) and arterial blood pressure (86 vs. 84 mm Hg). We speculate that physical factors relating to oxygen exchange may constrain general RBC velocity in capillaries to a certain range for optimum oxygen exchange, regardless of species.

© 2010 Elsevier B.V. All rights reserved.

1. Introduction

Red blood cells (RBCs) in single capillaries play a critical role in supplying neurons with oxygen, but literature values of their velocity are quite discrepant. Two-slit photometry and cross-correlation (Ma et al., 1974), high-speed microcinephotography (Pawlik et al., 1981), intravital microfilming (Ivanov et al., 1981), radioactive microspheres (Chang et al., 1984), a dual window technique with two fluorescent tracers (Yamaguchi et al., 1992), a dual window and cross-correlation method

* *Corresponding author.* Fax: +81 3 3353 1272.
E-mail address: nrsuzuki@sc.itc.keio.ac.jp (N. Suzuki).

Abbreviations: CBF, cerebral blood flow; FITC, fluorescein isothiocyanate; fps, frames per second; RBC, red blood cell; ROI, region of interest

[1] Present address: Division of Genomic Epidemiology, Department of Clinical Research and Informatics, International Medical Center of Japan, Tokyo, Japan.

0006-8993/$ – see front matter © 2010 Elsevier B.V. All rights reserved.
doi:10.1016/j.brainres.2010.01.032

(Hudetz, 1997a), laser-scanning confocal fluorescence microscopy (Seylaz et al., 1999) and two-photon laser-scanning microscopy (Hutchinson et al., 2006) have been employed to measure RBC velocity in microvessels of cerebral cortex of various species. The reported mean velocities center around 1 mm/s, with a range of 0.39 to 2.08 mm/s.

In previous communications, we have reported the detection of RBCs having much higher velocity than the above literature values in urethane-anesthetized rats, using a laser-scanning confocal microscope system with Matlab-domain tracking software, KEIO-IS2, developed by us (Schiszler et al., 2005; Tomita et al., 2008; Unekawa et al., 2008). The use of a high-speed camera (500 frames/s (fps)) was crucially important, since RBCs with relatively high velocities would have been missed in successive frames and would therefore have been uncounted in previous methods which employed conventional cameras with low frame rates (for example, 30 fps).

Recently, there has been a shift in animal experiments from the use of rats to mice, since the latter have a smaller body size and are convenient for the development of gene-recombination technologies. In the present work, we aimed to measure the velocities of RBCs in single capillaries in the mouse brain for comparison with those in rats, and further, to examine the characteristics of the RBC motion, including the frequency distribution function and fluctuations of RBC velocity in single capillaries.

2. Results

The body weight of mice is about one-tenth of that of rats (average body weight of the mice we used was 26.3±3.1 g, versus 327±32 g for Wistar rats). The diameter of mouse RBCs was slightly smaller (6.0 μm) than that of rat RBCs (6.5 μm) (unpublished observation with a VEC–DIC microscope). The heart rate of mice at the beginning of experiments was statistically significantly higher (461.4±50.5 bpm) than that of rats measured with the same apparatus (314.5±50.6 bpm) ($p<0.001$), although arterial blood pressures were similar (85.7±23.7 mm Hg in mice and 83.5±13.7 mm Hg in rats). Arterial blood pressure and heart rate were stable during the experiments.

In 21 mice, 726±614 RBCs per mouse (ranging from 72 to 1444) were detected as moving RBCs and 79±82 RBCs per mouse (ranging 5 to 262) were identified as flowing in single capillaries during the recording period (10 s) in the region of interest (ROI) of 500×500 μm. The total number of capillaries identified according to our criteria (see Experimental procedures) was 9.1±8.9 (per mouse, ranging 1 to 36) and the sum of the length of the detected capillaries was 635±563 μm per mouse (ranging 70 to 2320 μm). These numbers were similar to those of rats used in the previous experiments (Unekawa et al., 2008); namely, the measurement conditions and selected ROIs seem to be well matched in the different experiments.

As shown in Fig. 1, mean RBC velocity in single capillaries in each mouse was 2.16±1.31 mm/s with a range of 0.76 (minimum value) to 6.57 mm/s (maximum value). The mean velocity was not statistically significantly different from that in rats (2.20±1.59 mm/s, with a range of 0.93 to 4.06 mm/s).

The frequency distribution function of RBC velocities (h(v)) was obtained by stratifying velocity at every 0.5 mm/s and

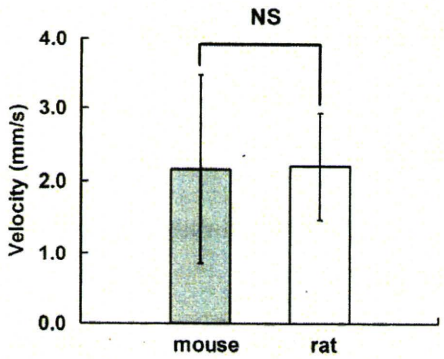

Fig. 1 – RBC velocity in single capillaries in mice (shadowed column, $n=21$) and rats (open column, $n=37$). Values are represented as mean±SD. The velocities in the two species were not significantly different ($p>0.05$). The values of rat RBC velocity are those reported previously (Unekawa et al., 2008).

counting the number of RBC appearances in the strata after integration of all RBC velocity data collected in a single capillary (Fig. 2). The total number of RBCs in capillaries was 1655 among the total of 15241 RBCs detected in all categories of vessels (arterioles, capillaries and venules) in the present experiments. The mean velocity of RBCs exclusively in single capillaries was 2.03±1.42 mm/s. This value was not statistically significantly different from the value in rats ($p>0.05$), even when we employed Mann–Whitney's U test or t-test after logarithmic conversion (the distribution curve was not a normal probability distribution). RBC velocities in capillaries were clustered at around 1.0 mm/s, tailing to higher velocities of up to 8.6 mm/s, and 59% of the RBCs in capillaries showed a velocity within the range of 0.5 to 2.0 mm/s. Moment analysis of the frequency distribution functions plotted against velocity (h(v)) in mice and rats revealed that the 4th moment,

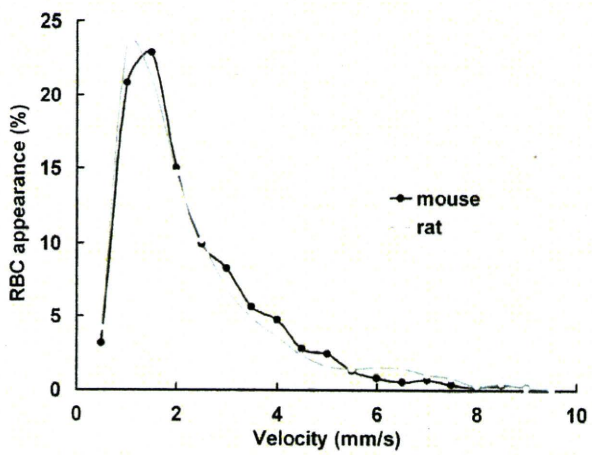

Fig. 2 – Frequency distribution function of RBC velocities in single capillaries in mice (closed circles and black lines, total number of RBCs=1655) and in rats (open circles and gray lines, total number of RBCs=4311). Each plot is shown as a percentage with respect to the total number of RBCs. The values of rat RBC velocity are those reported previously (Unekawa et al., 2008).

kurtosis, was 2.97 for mice and 2.78 for rats, respectively. The similarity of these higher moments further supports the similarity of the two curves.

We have demonstrated that capillary RBC velocity fluctuates temporally and spatially, and yet each capillary has a characteristic velocity (Unekawa et al., 2008). When capillaries in which RBCs were detected at least 5 times were selected, 1360 RBCs were obtained as flowing in 80 capillaries. The mean velocities of RBCs were calculated for the individual capillaries, and plotted as short horizontal bars with small dots representing each velocity (Fig. 3). The mean and standard deviation of the individual mean velocities in single capillaries were 1.76± 0.59 mm/s, again being not significantly different from those of rats (1.96±1.26 mm/s; previously presented data (Unekawa et al., 2008)). The average of the SD of RBC velocities in each capillary, a surrogate indicator of the individual fluctuations, was 0.34 mm/s (35.6% of the mean value), and this is also not significantly different from the average value of 0.59 mm/s (34.0%) in rats. It appears that RBC velocities in capillaries continually fluctuate within a limited range. The fluctuation was specific to individual capillaries, as was the case in rats.

3. Discussion

The present results demonstrate that the movements of RBCs in single capillaries in mice are quite similar to those in rats, notwithstanding the differences in RBC diameter, body size and heart rate. The average RBC velocity in mice is much faster than the previously reported value in intact capillaries of mouse cerebral cortex (0.53 mm/s) (Tomita et al., 2005) or in normal capillaries or neocapillaries generated on gel–nylon mesh (0.7–1.3 mm/s)(Nageswari et al., 2002; Niimi et al., 2000). This difference is considered to be due to the difference of frame rate or shutter speed of the camera in the recording system (30 fps in the literature vs 500 fps in the present experiments). Actually, RBC velocities of 1.1–2.08 mm/s were observed with a high frame rate (200–400 fps) in cats (Chang et al., 1984; Pawlik et al., 1981; Yamaguchi et al., 1992). We previously reported that there is a clear frame rate dependency of apparent RBC velocity; when higher frame rates are employed, higher mean RBC velocities are obtained, because rapidly moving RBCs can only be detected when a high-speed camera is used for analysis (Unekawa et al., 2008). Namely, rapidly moving RBCs are missing in successive frames at low frame rates, and are therefore uncounted. The lower values in the literature were all acquired at low frame rates.

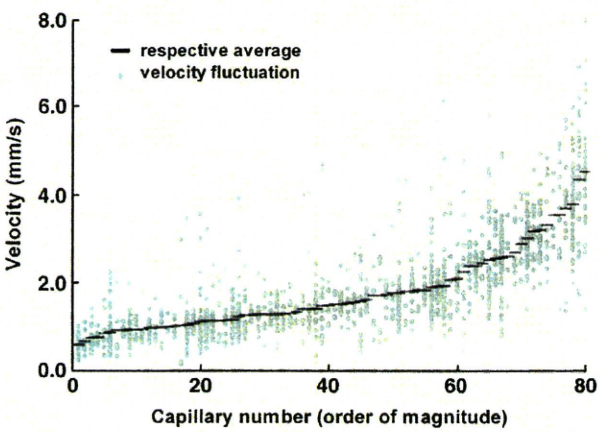

Fig. 3 – Fluctuation (gray dots) and respective averages (horizontal small bars) of RBC velocities in individual capillaries. Eighty capillaries, in which RBC tracks were detected 5 or more times, were selected in 21 mice and ranked in order of their average velocities. All fluctuating velocities were plotted against rank.

It may be thought that similar velocity of RBCs reflects a similar cerebral blood flow (CBF) in rodents. Absolute assessment of local CBF has been achieved by means of a ^{14}C-iodoantipyrine autoradiographic technique. Local CBF in the cerebral cortex under physiological conditions or at an intact site in partially ischemic mice is 70–150 ml/100 g/min (de Vasconcelos et al., 2005; Engel et al., 2008; Jiang et al., 2006; Kawai et al., 1997; Leithner et al., 2008; Lundblad and Bentzer, 2007; Niwa et al., 2001; Saleem et al., 2007), which is slightly higher than that of rats (45–145 ml/100 g/min) (Chi et al., 1999; Miyamoto and Auer, 2000; Narayanan et al., 2002; Takagi et al., 1995; Tanaka et al., 2001; Tohyama et al., 1997). On the other hand, lower CBF (25–50 ml/100 g/min) has been demonstrated in cats (Goadsby, 1989; Sutton et al., 1989). The regular relationship between resting metabolic rate, or rate of oxygen consumption, and the body size of an animal is well known. In most mammals, blood volume is a constant fraction of the body, but RBC size and capillary diameter are constant. In order to satisfy higher oxygen requirement, capillary density must be higher (shorter diffusion distance) in small animals (Schmidt-Nielsen, 1984). Therefore, it is reasonable that blood flow per a gram tissue is higher in small animals. Furthermore, diversity of CBF might be due to strain difference or be influenced by the mode of anesthesia. We used inhalation of isoflurane in mice and intraperitoneal administration of urethane in rats. Nevertheless, the essentially identical velocity characteristics, especially the frequency distribution function, of RBCs in mice and rats seem noteworthy.

The responses of CBF to hypercapnia was much higher than the response of RBC velocity (Hudetz, 1997b). The onset and the peak increases in RBC velocity to neuronal activation in response to hind paw stimulation were not corresponded to those of CBF, suggesting that the capillary and arteriole are controlled by independent mechanisms (Matsuura et al., 1999). Cortical spreading depression induced periodic decreases in both RBC number and velocity until RBCs halted or disappeared (Tomita et al., 2009). RBC velocity in capillaries remained broadly unchanged, whereas RBC number (appearance) decreased by topical application or intravenous administration of nitroprusside, whereas microflow markedly increased (Tomita et al., in press). The area of usual CBF measurement is rather large (for example, 1 mm^3 with laser Doppler flowmetry) and the obtained values are the average in the area containing arterioles, venules, and so on. But our results of RBC velocity are only in capillaries, excluding such vessels. Thus, we consider that RBC velocity in capillaries and CBF are not always regulated by a single or simple mechanism.

Generally, the specific metabolic rate increases as the animal body weight decreases. CBF also scales with body size

as mentioned above. It represents that the smaller the animal, the higher the volume rate of blood flow. Mammalian cerebral blood volume appears to be constant, resulting that mean transit time should decrease with decreasing brain size (Shockley and LaManna, 1988). Therefore, since the RBC velocity distribution of mice is similar with that of rats, the capillary length may be shorter in smaller animals. However, the detected length of capillaries of mice was comparative with that of rats in this experiment. Mean transit time is also proportional to the ratio of blood volume to blood flow, according to Stewart–Hamilton equation. The length of the capillaries, which was identified with Matlab domain KEIO-IS2, and calculated mean transit time in mice were comparative with those in rats in this experiment. Furthermore, similar RBC velocity and increased oxygen consumption may show oxygen delivery is facilitated in the smaller animals.

RBC velocity in cerebrocortical capillaries of other species has been estimated as around 1 mm/s. However, there are methodological difficulties and ethical problems in directly observing capillaries in human brain. Packed RBC volume, red cell size, capillary diameter, blood gases and blood pressure are fairly constant across mammalian species. Scaling lows of the complex branching pattern and vascular tree structure have been shown to be deduced on the basis of the minimum energy hypothesis and conservation of energy under steady state conditions (Kassab, 2006). We hypothesize that general RBC velocity in capillaries is limited to a certain range by physical factors related to the requirements for optimum oxygen extraction, regardless of species.

4. Experimental procedures

Twenty-one C57BL/6J mice (8–10 weeks old, body weight, 26.3±3.1 g) were used with the approval (# 071095) of the Animal Ethics Committee of Keio University, and all experimental procedures were in accordance with the university's guidelines for the care and use of laboratory animals. Under anesthesia with isoflurane (ca. 1.5%) administered via a concentration-controllable anesthesia unit (400, Univentor Ltd., Zejtun, Malta), each mouse was fixed to a head-holder and a cranial window of approximately 3 mm in diameter was opened in the left side of the skull at the parieto-temporal region of the cerebral cortex. The dura was kept intact and the exposed cortex was covered with a cover slip to prevent it from drying out. A tail vein was catheterized to intravenously inject various solutions. An appropriate capillary-rich ROI in the cerebral cortex was selected, and 0.05 ml of fluorescein isothiocyanate (FITC)-labeled RBC suspension, prepared beforehand according to Seylaz et al. (Seylaz et al., 1999), was injected into the bloodstream through the venous catheter. Fall of body temperature was prevented with a heating-pad and thermo-controller (BWT-100, Bioresearch Center Co., Ltd., Nagoya, Japan). In some experiments, arterial blood pressure and heart rate were recorded with an intermittent cuff method applied to the hindlimb (a non-invasive blood pressure monitor; MK-200, Muromachi Kikai Co., Ltd., Tokyo, Japan). The methods of measurement of RBC velocity using the high-speed camera (500 fps) laser-scanning confocal fluorescence microscope and the image analyzing system with a MATLAB® (The Math Works, Inc., Natick, MA, USA) environment with application software (KEIO-IS2) developed in our laboratory (Schiszler et al., 2005) were reported elsewhere (Tomita et al., 2008; Unekawa et al., 2008). With reference to the alternatively recorded images obtained using a conventional video camera, we defined single capillaries as having a diameter less than 10 μm, based on other reports (Hutchinson et al., 2006; Williams et al., 1993). The frequency distribution function was obtained by stratification of velocities at every 0.5 mm/s and counting the appearance of RBCs within the range. The characteristics of RBC velocities in mice were compared with reported data for rats (Unekawa et al., 2008).

Data in text and figures are presented as mean±standard deviation (SD). Non-paired Student's *t*-test was performed to assess statistical significance, except where otherwise noted in the text.

Acknowledgments

The authors thank Prof. Susumu Terakawa (Photon Medical Research Center, Hamamatsu University School of Medicine, Japan) for determination of the size of RBCs. This work was supported by JSPS Grant-in-Aid # 17390255 (Suzuki, N) and # 19591008 (Tomita, Y). The authors also thank Otsuka Pharmaceutical Co., Ltd., Novartis Pharma K.K. and Pfizer Japan Inc. for financial supports.

REFERENCES

Chang, B.L., Santillan, G., Bing, R.J., 1984. Red cell velocity and autoregulation in the cerebral cortex of the cat. Brain Res. 308, 15–24.

Chi, O.Z., Chang, Q., Wang, G., Liu, X., Weiss, H.R., 1999. A nonNMDA antagonist, GYKI 52466 improves microscopic O_2 balance in the cortex during focal cerebral ischemia. Neurol. Res. 21, 299–304.

de Vasconcelos, A.P., Bouilleret, V., Riban, V., Wasterlain, C., Nehlig, A., 2005. Role of nitric oxide in cerebral blood flow changes during kainate seizures in mice: genetic and pharmacological approaches. Neurobiol. Dis. 18, 270–281.

Engel, D.C., Mies, G., Terpolilli, N.A., Trabold, R., Loch, A., De Zeeuw, C.I., Weber, J.T., Maas, A.I., Plesnila, N., 2008. Changes of cerebral blood flow during the secondary expansion of a cortical contusion assessed by ^{14}C-iodoantipyrine autoradiography in mice using a non-invasive protocol. J. Neurotrauma 25, 739–753.

Goadsby, P.J., 1989. Effect of stimulation of facial nerve on regional cerebral blood flow and glucose utilization in cats. Am. J. Physiol. 257, R517–R521.

Hudetz, A.G., 1997a. Blood flow in the cerebral capillary network: a review emphasizing observations with intravital microscopy. Microcirculation 4, 233–252.

Hudetz, A.G., 1997b. Regulation of oxygen supply in the cerebral circulation. Adv. Exp. Med. Biol. 428, 513–520.

Hutchinson, E.B., Stefanovic, B., Koretsky, A.P., Silva, A.C., 2006. Spatial flow-volume dissociation of the cerebral microcirculatory response to mild hypercapnia. Neuroimage 32, 520–530.

Ivanov, K.P., Kalinina, M.K., Levkovich Yu, I., 1981. Blood flow velocity in capillaries of brain and muscles and its physiological significance. Microvasc. Res. 22, 143–155.

Jiang, W., Gu, W., Hossmann, K.A., Mies, G., Wester, P., 2006. Establishing a photothrombotic 'ring' stroke model in adult mice with late spontaneous reperfusion: quantitative

measurements of cerebral blood flow and cerebral protein synthesis. J. Cereb. Blood Flow Metab. 26, 927–936.
Kassab, G.S., 2006. Scaling laws of vascular trees: of form and function. Am. J. Physiol. Heart Circ. Physiol. 290, H894–H903.
Kawai, N., Keep, R.F., Betz, A.L., 1997. Hyperglycemia and the vascular effects of cerebral ischemia. Stroke 28, 149–154.
Leithner, C., Gertz, K., Schrock, H., Priller, J., Prass, K., Steinbrink, J., Villringer, A., Endres, M., Lindauer, U., Dirnagl, U., Royl, G., 2008. A flow sensitive alternating inversion recovery (FAIR)-MRI protocol to measure hemispheric cerebral blood flow in a mouse stroke model. Exp. Neurol. 210, 118–127.
Lundblad, C., Bentzer, P., 2007. Effects of L-arginine on cerebral blood flow, microvascular permeability, number of perfused capillaries, and brain water content in the traumatized mouse brain. Microvasc. Res. 74, 1–8.
Ma, Y.P., Koo, A., Kwan, H.C., Cheng, K.K., 1974. On-line measurement of the dynamic velocity of erythrocytes in the cerebral microvessels in the rat. Microvasc. Res. 8, 1–13.
Matsuura, T., Fujita, H., Seki, C., Kashikura, K., Yamada, K., Kanno, I., 1999. CBF change evoked by somatosensory activation measured by laser-Doppler flowmetry: independent evaluation of RBC velocity and RBC concentration. Jpn. J. Physiol. 49, 289–296.
Miyamoto, O., Auer, R.N., 2000. Hypoxia, hyperoxia, ischemia, and brain necrosis. Neurology 54, 362–371.
Nageswari, K., Yamaguchi, S., Yamakawa, T., Niimi, H., 2002. Quantitative assessment of cerebral neocapillary network and its remodeling in mice using intravital fluorescence videomicroscopy. Angiogenesis 5, 99–105.
Narayanan, U., Weiss, H.R., Liu, X., Chi, O.Z., 2002. Exogenous endothelin-1 improves microvascular oxygen balance during focal cerebral ischemia in the rat. Regul. Pept. 105, 1–7.
Niimi, H., Nageswari, K., Ranade, G., Yamaguchi, S., Yamakawa, T., 2000. Microcirculatory characterization of cerebral angiogenesis in mice using intravital videomicroscopy. Clin. Hemorheol. Microcirc. 23, 293–301.
Niwa, K., Haensel, C., Ross, M.E., Iadecola, C., 2001. Cyclooxygenase-1 participates in selected vasodilator responses of the cerebral circulation. Circ. Res. 88, 600–608.
Pawlik, G., Rackl, A., Bing, R.J., 1981. Quantitative capillary topography and blood flow in the cerebral cortex of cats: an in vivo microscopic study. Brain Res. 208, 35–58.
Saleem, S., Li, R.C., Wei, G., Dore, S., 2007. Effects of EP1 receptor on cerebral blood flow in the middle cerebral artery occlusion model of stroke in mice. J. Neurosci. Res. 85, 2433–2440.
Schiszler, I., Takeda, H., Tomita, M., Tomita, Y., Osada, T., Unekawa, M., Tanahashi, N., Suzuki, N., 2005. Software (KEIO-IS2) for automatically tracking red blood cells (RBCs) with calculation of individual RBC velocities in single capillaries of rat brain. J. Cereb. Blood. Flow Metab. 25 (suppl), S541.
Schmidt-Nielsen, K., 1984. Scaling, Why is Animal Size so Important? Cambridge University Press, Cambridge, New York.
Seylaz, J., Charbonné, R., Nanri, K., Von Euw, D., Borredon, J., Kacem, K., Méric, P., Pinard, E., 1999. Dynamic in vivo measurement of erythrocyte velocity and flow in capillaries and of microvessel diameter in the rat brain by confocal laser microscopy. J. Cereb. Blood Flow Metab. 19, 863–870.
Shockley, R.P., LaManna, J.C., 1988. Determination of rat cerebral cortical blood volume changes by capillary mean transit time analysis during hypoxia, hypercapnia and hyperventilation. Brain Res. 454, 170–178.
Sutton, L.N., Barranco, D., Greenberg, J., Dante, S., Florin, S., Welsh, F., 1989. Cerebral blood flow and glucose metabolism in experimental brain edema. J. Neurosurg. 71, 868–874.
Takagi, K., Zhao, W., Busto, R., Ginsberg, M.D., 1995. Local hemodynamic changes during transient middle cerebral artery occlusion and recirculation in the rat: a [^{14}C]iodoantipyrine autoradiographic study. Brain Res. 691, 160–168.
Tanaka, K., Nogawa, S., Ito, D., Suzuki, S., Dembo, T., Kosakai, A., Fukuuchi, Y., 2001. Phosphorylation of cyclic adenosine monophosphate response element binding protein in oligodendrocytes in the corpus callosum after focal cerebral ischemia in the rat. J. Cereb. Blood Flow Metab. 21, 1177–1188.
Tohyama, Y., Sako, K., Yonemasu, Y., 1997. Protein kinase C in focal ischemic rat brain: dual autoradiographic analysis of [^{14}C] iodoantipyrine (IAP) and [^{3}H]phorbol-12, 13-dibutyrate (PDBu). Brain Res. 750, 155–160.
Tomita, Y., Kubis, N., Calando, Y., Tran Dinh, A., Meric, P., Seylaz, J., Pinard, E., 2005. Long-term in vivo investigation of mouse cerebral microcirculation by fluorescence confocal microscopy in the area of focal ischemia. J. Cereb. Blood Flow Metab. 25, 858–867.
Tomita, M., Osada, T., Schiszler, I., Tomita, Y., Unekawa, M., Toriumi, H., Tanahashi, N., Suzuki, N., 2008. Automated method for tracking vast numbers of FITC-labeled RBCs in microvessels of rat brain in vivo using a high-speed confocal microscope system. Microcirculation 15, 163–174.
Tomita, M., Tomita, Y., Toriumi, H., Unekawa, M., Suzuki, N., 2009. Coupling of capillary RBC flow failure with neuronal depolarization. Nature Proceedings. [The data are available at http://precedings.nature.com/documents/3220/version/1].
Tomita, M., Osada, T., Unekawa, M., Tomita, Y., Toriumi, H., Suzuki, N., in press. Exogenous nitric oxide increases microflow but decreases RBC attendance in single capillaries in rat cerebral cortex. Microvasc. Rev. Commun.
Unekawa, M., Tomita, M., Osada, T., Tomita, Y., Toriumi, H., Tatarishvili, J., Suzuki, N., 2008. Frequency distribution function of red blood cell velocities in single capillaries of the rat cerebral cortex using intravital laser-scanning confocal microscopy with high-speed camera. Asian Biomed. 2, 203–218.
Williams, J.L., Shea, M., Jones, S.C., 1993. Evidence that heterogeneity of cerebral blood flow does not involve vascular recruitment. Am. J. Physiol. 264, H1740–H1743.
Yamaguchi, S., Yamakawa, T., Niimi, H., 1992. Red cell velocity and microvessel diameter measurement by a two fluorescent tracer method under epifluorescence microscopy: application to cerebral microvessels of cats. Int. J. Microcirc. Clin. Exp. 11, 403–416.

American Journal of Epidemiology
© The Author 2010. Published by Oxford University Press on behalf of the Johns Hopkins Bloomberg School of Public Health. All rights reserved. For permissions, please e-mail: journals.permissions@oxfordjournals.org.
Vol. 172, No. 9
DOI: 10.1093/aje/kwq281
Advance Access publication: September 16, 2010

Original Contribution

Association of a Cyclin-Dependent Kinase 5 Regulatory Subunit-Associated Protein 1-Like 1 (*CDKAL1*) Polymorphism With Elevated Hemoglobin A_{1c} Levels and the Prevalence of Metabolic Syndrome in Japanese Men: Interaction With Dietary Energy Intake

Koichi Miyaki, Than Oo, Yixuan Song, Htay Lwin, Yutaka Tomita, Haruhiko Hoshino, Norihiro Suzuki, and Masaaki Muramatsu*

* Correspondence to Dr. Masaaki Muramatsu, Department of Molecular Epidemiology, Medical Research Institute, Tokyo Medical and Dental University, 2-3-10 Kandasurugadai, Chiyoda-ku, Tokyo 101-0062, Japan (e-mail: muramatsu.epi@mri.tmd.ac.jp).

Initially submitted May 18, 2009; accepted for publication March 30, 2010.

Genome-wide association studies have identified the cyclin-dependent kinase 5 regulatory subunit-associated protein 1-like 1 (*CDKAL1*) gene as a novel risk factor for type 2 diabetes mellitus. Application of this genetic marker for prevention of type 2 diabetes and metabolic syndrome (MetS) in healthy populations has not yet been evaluated. The authors examined the effects of a *CDKAL1* polymorphism (rs9465871) on metabolic phenotype and of gene-lifestyle (*CDKAL1*-energy intake) interaction on MetS in a cohort of apparently healthy Japanese men examined in 2003. The CC genotype of the *CDKAL1* variant was associated with elevated glycosylated hemoglobin A_{1c} (HbA1c) levels. The prevalence of MetS was 25.6% for CC and 16.3% for TT + CT (odds ratio = 2.18, 95% confidence interval: 1.06, 4.48; $P = 0.035$). When dietary energy intake was accounted for, the variant's effect on HbA1c was observed in the highest energy-intake group (mean: CC, 5.6% (standard deviation, 1.7); TT + CT, 5.0% (standard deviation, 0.5); $P = 0.025$). In addition, the positive association between HbA1c and energy intake was stronger in subjects with the CC genotype than in subjects with TT + CT. These results suggest that the interaction between the *CDKAL1* polymorphism and dietary energy intake influences the dysglycemic phenotype leading to MetS, possibly through impaired insulin secretion. The *CDKAL1* polymorphism may be a marker for MetS in the Japanese population.

CDKAL1 protein, human; energy intake; hemoglobin A1c protein, human; Japan; metabolic syndrome X

Abbreviations: CDK5, cyclin-dependent kinase 5; CDKAL1, CDK5 regulatory subunit-associated protein 1-like 1; HbA1c, hemoglobin A_{1c}; MetS, metabolic syndrome; PCR, polymerase chain reaction; SD, standard deviation.

***Editor's note**: An invited commentary on this article appears on page 992, and the authors' response appears on page 998.*

Metabolic syndrome (MetS) is characterized by abdominal obesity, hypertension, dyslipidemia, and glucose intolerance (1) and is considered a serious health hazard in developed countries. MetS occurs in up to 22% and 14.7% of US and Japanese adults, respectively (2, 3). In addition, MetS is an independent predictor of the development of type 2 diabetes mellitus and cardiovascular disease (4, 5). The development and progression of MetS is probably affected by a complex interaction of genetic and environmental factors, but the genetic factors that influence MetS remain mostly unknown. However, certain genetic factors affecting MetS may play a role in obesity, inflammation, insulin resistance, and/or glucose and lipoprotein metabolism (6). Our previous studies showed that a gene altered during inflammation, interleukin 6 receptor (*IL6R*), and a gene altered due to obesity, cell death-inducing DNA fragmentation factor α-like effector A (*CIDEA*), are both associated with MetS (7, 8).

Downloaded from aje.oxfordjournals.org at Keio University (PULC Consortium) on November 24, 2010

Recently, genome-wide association studies identified multiple gene products involved in polygenic diseases, such as type 2 diabetes; cyclin-dependent kinase 5 (CDK5) regulatory subunit-associated protein 1-like 1 (*CDKAL1*) was identified by the Wellcome Trust Case-Control Consortium for its association with type 2 diabetes (9). Subsequent studies in different populations have successively corroborated this association, and *CDKAL1* is now considered to have a bona fide association with type 2 diabetes in both Western and Japanese populations (10–16). The whole-genome approach is useful for identifying new markers of genetic associations, but determining the effect under the influence of lifestyle factors, such as energy intake, is important. Genome-wide association studies and replication studies have confirmed *CDKAL1* as a genetic marker in several European populations, but there have been only a few replication studies in Japanese. Takeuchi et al. (13) reported that *CDKAL1* is the best-replicated susceptibility locus and the strongest associated with type 2 diabetes among several susceptibility loci, including *KCNQ1* (potassium voltage-gated channel, KQT-like subfamily, member 1), in the Japanese population. Recent studies have shown that type 2 diabetes has a strong positive correlation with total energy intake, which could be a more significant risk factor for type 2 diabetes (17, 18). In addition, the gene-lifestyle (*CDKAL1*-energy intake) interaction effect on type 2 diabetes and MetS has not yet been examined in the Japanese population. Therefore, we studied the effect of this genetic marker, the *CDKAL1* polymorphism, to determine whether it affects the glycemic phenotype, as well as the effect of the gene-lifestyle interaction on MetS in apparently healthy Japanese.

CDKAL1 is expressed in human pancreatic islet cells and shares homology with CDK5 regulatory subunit-associated protein 1, an inhibitor of CDK5 (10). CDK5 has been reported to regulate insulin secretion (19) and maintain β-cell function under glucotoxic conditions (20). Thus, *CDKAL1* probably plays a role in the regulation of insulin secretion from pancreatic β cells, even under glucotoxic conditions.

To the best of our knowledge, no one has reported an interaction effect of the *CDKAL1* polymorphism and lifestyle-related energy intake on type 2 diabetes and MetS, since the pathogenesis of MetS is likely to be affected by gene-lifestyle interactions. We investigated whether *CDKAL1* is associated with MetS and whether an interaction effect of this polymorphism and energy intake on MetS is present in healthy Japanese men.

MATERIALS AND METHODS

Study subjects

A total of 313 male Japanese workers from Kanagawa Prefecture, Japan, underwent a health examination in 2003 and were enrolled in this study. Written informed consent was obtained from each participant. Detailed descriptions of the participants are provided elsewhere (7, 8). The mean age and body mass index (weight (kg)/height $(m)^2$) of the participants were 45.7 years (standard deviation (SD), 11.7) and 23.4 (SD, 3.5), respectively. Fifty-eight subjects (18.5%) were diagnosed with MetS, among whom 7 were treated with antidiabetes medication and 37 were treated with antihypertensive medication. The present study was approved by the Ethics Review Committee of the Medical Research Institute of Tokyo Medical and Dental University. MetS was defined according to the criteria of the Japanese Society of Internal Medicine (21) for men as a waist circumference of ≥85 cm and 2 or more of the following: 1) dyslipidemia, serum triglyceride level ≥150 mg/dL, and/or high density lipoprotein cholesterol level <40 mg/dL; 2) high blood pressure (systolic blood pressure ≥130 mmHg or diastolic blood pressure ≥85 mm Hg); and 3) impaired fasting glucose concentration (≥110 mg/dL).

Phenotype measurements

Height, weight, systolic blood pressure, and diastolic blood pressure were measured for each participant. All subjects fasted for 12 hours before blood collection. Plasma glucose, serum glycosylated hemoglobin A_{1c} (HbA1c), serum triglyceride, total cholesterol, and high density lipoprotein cholesterol levels were measured. Body mass index was calculated as weight (kg) divided by height squared (m^2). Data on the participants' age, family history of diabetes, and current smoking and alcohol drinking status were obtained using a self-reported questionnaire. Dietary energy intake was calculated from a validated semiquantitative food frequency questionnaire, which was evaluated by a comparison with the 7-day dietary records of 66 subjects (22). The multiple correlation coefficients (R^2) for correlation between the 2 methods were 0.217, 0.173, 0.150, and 0.238 for energy, protein, lipids, and carbohydrates, respectively (22). The food frequency questionnaire method has been previously described in detail (7, 8, 23). We classified the subjects into tertile groups based on their energy intake levels in order to obtain an approximate number of subjects for the comparative analysis: low, 2,474.5–6,788.6 kJ/day; middle, 6,790.3–8,465.6 kJ/day; and high, 8,499.9–17,740.0 kJ/day.

DNA genotyping

Peripheral blood was drawn from each subject, and genomic DNA was extracted using a standard method (7, 8). The *CDKAL1* polymorphism rs9465871, which is in very high linkage disequilibrium with the rs7756992 polymorphism ($D' = 1.0, r^2 = 0.91$) used in replication studies (12), was selected on the basis of previous genome-wide association studies by the Wellcome Trust Case-Control Consortium (for the association with type 2 diabetes, genotype P value $= 3.34 \times 10^{-7}$) (9). The analysis of rs9465871 was performed by polymerase chain reaction (PCR), followed by a melting curve analysis using the LightCycler 480 System (Roche Diagnostics, Penzberg, Germany). PCR primers and hybridization probes used were as follows: 5′-CAG TAG AGG TGG AGG AAG-3′ (sense primer), 5′-TCA TCA GAA CAA CCA CCA GT-3′ (antisense primer), 5′-GCA TGT TTC CAG AAG GAG GAG TGA TCA GCT GTG TA-3′ conjugated to fluorescein (sensor probe), and 5′-LC Red 640-GTG TTG CTG AGA AAC TGA GTT AGA T-Phosphate (anchor probe). PCR was performed in a reaction

Downloaded from aje.oxfordjournals.org at Keio University (PULC Consortium) on November 24, 2010

mixture containing 0.05 μM sense primer, 0.5 μM antisense primer, 0.2 μM anchor probe, 0.2 μM sensor probe, 10 ng of genomic DNA, and 1 μL of 5X LightCycler 480 genotyping master solution (modified *Taq* DNA polymerase, reaction buffer, dNTP mix, and 15 mM magnesium chloride) in a total volume of 5 μL. The reaction parameters consisted of a 10-minute initial denaturation at 95°C followed by 45 cycles of denaturation at 95°C for 15 seconds, annealing at 55°C for 15 seconds, and extension at 72°C for 15 seconds. After PCR amplification, a melting curve analysis was performed by the reaction's being held at 95°C for 1 minute and at 40°C for 1 minute and then slowly heated to 85°C with a ramp rate of 2°C per second. The melting curve data were collected and classified using the LightCycler genotyping software.

Statistical analysis

The allele frequency was calculated, and the deviation of the genotype distribution from Hardy-Weinberg equilibrium was determined using a chi-square test. Analysis of variance with or without adjustment (age and height) was used to compare the mean values of basic and clinical characteristics and energy intake levels among genotype groups. The odds ratio and 95% confidence interval for the prevalence of MetS between different genotype groups was evaluated using a multiple logistic regression model with or without adjustment for age and height. Furthermore, the correlations between HbA1c level (a continuous variable) and *CDKAL1* genotype among the energy intake groups, or the energy intake levels among the genotype groups, were examined by multiple linear regression analyses, which were also adjusted for age, height, or current smoking and alcohol drinking status. Seven subjects were excluded because of antidiabetes treatment. Analysis of covariance was used to examine the gene-environment interaction effects on HbA1c and fasting blood glucose level. SPSS for Windows, version 11.0 (SPSS Inc., Chicago, Illinois), was used for all analyses. A P value less than 0.05 was considered significant. The corrected significance threshold level using the Bonferroni method, based on these 2 interaction tests, was $P = 0.05/2 = 0.025$). Although we analyzed the gene-environment interaction effect on the blood glucose level, we discuss the effect related to HbA1c rather than to fasting blood glucose.

RESULTS

The frequency of the minor allele, C, was 0.492, which was similar to the frequency in the Japanese general population (0.456; http://www.hapmap.org/). The frequencies of the CC, CT, and TT genotypes of rs9465871 among the 313 Japanese men were 25.2%, 47.9%, and 26.8%, respectively. The genotype distribution did not deviate from Hardy-Weinberg equilibrium ($P = 0.46$).

Subjects were characterized according to age, height, body weight, body mass index, waist circumference, blood pressure, serum lipid level, fasting plasma glucose concentration, and HbA1c level and were categorized into 3 groups based on their genotype: CC, CT, and TT. There was no significant linear trend for the mean age- and height-adjusted differences in age, body weight, body mass index, waist circumference, systolic blood pressure, diastolic blood pressure, serum lipids, fasting plasma glucose, HbA1c, or age-adjusted height among the 3 *CDKAL1* genotype groups (data not shown). The adjusted mean HbA1c level in the CC genotype group (5.2% (SD, 1.2)) was higher than that in the CT group (5.0% (SD, 0.85); $P = 0.10$) or the TT group (4.99% (SD, 0.60)), but the difference was not significant ($P = 0.07$). Thus, we further classified the participants into 2 groups: TT + CT and CC, which was the homozygous recessive genotype associated with type 2 diabetes (9) and impaired fasting glucose in the previous replication study (24). We found no significant differences in age, height, body weight, body mass index, waist circumference, systolic blood pressure, diastolic blood pressure, serum lipid, or fasting plasma glucose levels between the TT + CT and CC genotype groups, even after adjustment for relevant confounding variables (Table 1). In addition, we found no significant differences for the lifestyle factors of dietary energy intake and current smoking and alcohol drinking status when comparing the TT + CT and CC genotype groups (Table 1). However, HbA1c levels were significantly higher in the CC group than in the TT + CT group ($P = 0.04$). Even after we excluded the 7 subjects with diabetes, carriers of the CC genotype had a significantly higher mean HbA1c level than persons with the TT + CT genotype ($P = 0.039$, linear regression) after adjustment for age, height, current smoking and drinking status, and energy intake.

The prevalence of MetS was also significantly different between the 2 *CDKAL1* genotype groups, with a prevalence of 25.6% in the CC group and 16.3% in the TT + CT group. After adjustment for age and height, the odds ratio for the CC group as compared with the TT + CT group was 2.18 (95% confidence interval: 1.06, 4.48) ($P = 0.035$).

We examined not only HbA1c but also fasting glucose concentration according to *CDKAL1* genotype. We did not find a significant relation between fasting glucose level and the *CDKAL1* variants (data not shown).

When analyzing the HbA1c levels of the CC and TT + CT groups after adjusting for age, height, and current smoking and drinking status and after grouping the subjects according to their dietary energy intake, we found the HbA1c level of the CC group with the highest energy intake to be significantly higher than that of the TT + CT group (5.6% (SD, 1.7) vs. 5.0% (SD, 0.5), $P = 0.025$; Figure 1). No such difference in HbA1c levels was found in the low-energy-intake group (CC vs. TT + CT: 4.9% (SD, 0.7) vs. 5.1% (SD, 1.1), $P = 0.99$; Figure 1) or the middle-energy-intake group (CC vs. TT + CT: 5.2% (SD, 0.9) vs. 4.9% (SD, 0.4), $P = 0.37$; Figure 1). Furthermore, the HbA1c level was also significantly different after accounting for the interaction between energy intake as a categorical variable and *CDKAL1* genotype ($P = 0.028$) and after adjusting for age, height, and current smoking and drinking status. The significant interaction effect ($P = 0.028$) was marginally greater than the conservative, Bonferroni-corrected effect ($P = 0.025$).

We also examined the correlation between HbA1c levels and energy intake in subjects with the CC and TT + CT genotypes. The TT + CT group did not show significant

Downloaded from aje.oxfordjournals.org at Keio University (PULC Consortium) on November 24, 2010

Table 1. Characteristics of Subjects According to Cyclin-Dependent Kinase 5 Regulatory Subunit-Associated Protein 1-Like 1 (*CDKAL1*) Genotype, Japan, 2003

	Genotype				*P* Value[a]
	CC (n = 79)		TT + CT (n = 234)		
	Mean (SD)	%	Mean (SD)	%	
Age, years	45.5 (11.7)		45.8 (11.7)		0.82
Height, cm	168.1 (6.8)		168.9 (6.1)		0.29
Body weight, kg	66.0 (10.3)		66.8 (11.5)		0.55
Body mass index[b]	23.4 (3.4)		23.4 (3.6)		0.90
Waist circumference, cm	83.6 (9.6)		83.9 (9.7)		0.75
Serum total cholesterol, mg/dL	208.6 (41.6)		206.3 (35.6)		0.68
Serum triglycerides, mg/dL	137.8 (87.5)		131.6 (81.9)		0.27
Serum high density lipoprotein cholesterol, mg/dL	52.9 (13.1)		56.2 (14.3)		0.07
Fasting plasma glucose, mg/dL	101.3 (34.6)		100.4 (33.4)		0.68
Serum hemoglobin A1c, %	5.2 (1.2)		5.0 (0.8)		0.04*
Systolic blood pressure, mm Hg	132.2 (18.8)		135.2 (17.5)		0.21
Diastolic blood pressure, mm Hg	79.5 (13.5)		82.4 (12.2)		0.09
Energy intake, kJ/day	7,700.8 (1,886.1)		7,724.0 (2,064.1)		0.76
Current smoking		57.5		60.8	0.62
Current alcohol consumption		69.9		74.5	0.44
Family history of diabetes		17.9		14.1	0.46
Prevalence of metabolic syndrome		25.6		16.3	0.035*

Abbreviations: ANOVA, analysis of variance; SD, standard deviation.

* $P < 0.05$.

[a] P values were derived using an additive model and were determined by unadjusted ANOVA (age), ANOVA adjusted for age (height), ANOVA adjusted for age and height (other continuous traits), or chi-square test (categorized traits).

[b] Weight (kg)/height $(m)^2$.

positive correlations between HbA1c and energy intake, but the CC group did show a correlation (Figure 2). In the TT + CT group, the regression coefficient was 0.16, and P equaled 0.012 for the trend after adjustment for age, height, and smoking and drinking status (Figure 2A). In the CC group, the regression coefficient was 0.25 and P was 0.037 for the trend (Figure 2B). Furthermore, when we examined the interaction term for *CDKAL1* genotype and energy intake using the multivariate-adjusted general linear model and adjusted for age, height, and current smoking and drinking status, the positive correlation between HbA1c and energy intake was significantly greater in the CC genotype group than in the TT + CT genotype group ($P < 0.001$; Figure 2C). These results indicate that HbA1c levels tend to be higher in subjects with the CC genotype than in those with the TT + CT genotype when energy intake is higher.

DISCUSSION

The present study showed that a polymorphism in the type 2 diabetes risk-conferring *CDKAL1* gene is associated with elevated HbA1c levels and an increased prevalence of MetS in apparently healthy Japanese men. The risk allele and genetic models were the same as in the previous study of type 2 diabetes (9).

HbA1c is a minor component of hemoglobin, and the proportion of HbA1c in total hemoglobin (%) is considered to be an integrated measure of blood glucose concentrations for 6–8 weeks prior to HbA1c measurement (25). Therefore, HbA1c is widely accepted as a standard method for determining long-term glycemic control in diabetic patients (26). HbA1c has also been suggested to serve as a predictor of progression to type 2 diabetes in nondiabetic persons (27, 28), as well as for MetS (29). Sung et al. (29) reported that an HbA1c level of 5.5% represents the value with maximum sensitivity and specificity for the diagnosis of MetS in a large-scale cross-sectional study among nondiabetic South Korean adults. In addition, an HbA1c level of 5.2% or less has been recommended in recent guidelines from the Japanese Ministry of Health, Labour, and Welfare (30) to aid in the diagnosis of MetS. Therefore, although the current effect of *CDKAL1* variants on HbA1c levels is within the normal range and is modest (CC vs. TT + CT: 5.2% (SD, 1.2) vs. 5.0% (SD, 0.8)), we think that this difference is an indication of a subtle dysglycemic phenotype detected prior to the elevation in

Downloaded from aje.oxfordjournals.org at Keio University (PULC Consortium) on November 24, 2010

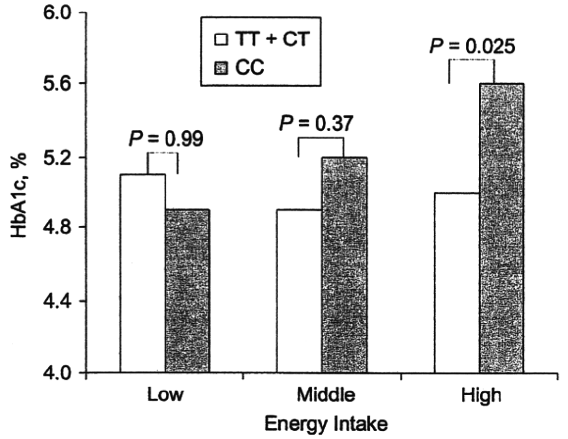

Figure 1. Mean hemoglobin A_{1c} (HbA1c) level according to cyclin-dependent kinase 5 regulatory subunit-associated protein 1-like 1 (*CDKAL1*) genotype, Japan, 2003. Subjects were further grouped by tertile of energy intake (low (2,474.5–6,788.6 kJ/day), middle (6,790.3–8,465.6 kJ/day), or high (8,499.9–17,740.0 kJ/day)), with adjustment for age, height, and current smoking and alcohol drinking status. The HbA1c level of the CC group with the highest energy intake was significantly higher than that of the TT + CT group.

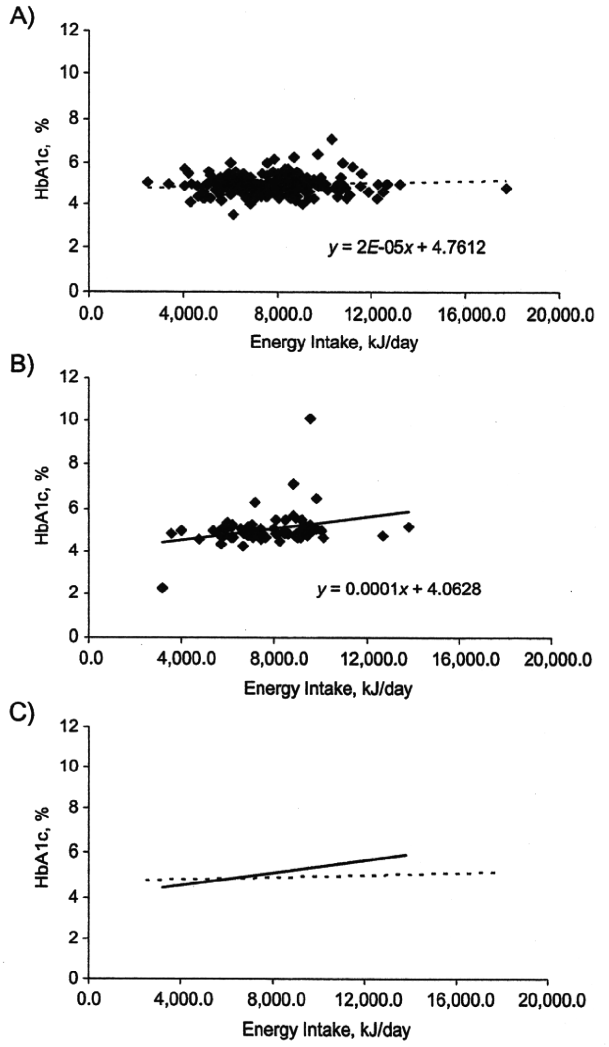

Figure 2. Effects of daily energy intake on hemoglobin A_{1c} (HbA1c) level in subjects with different cyclin-dependent kinase 5 regulatory subunit-associated protein 1-like 1 (*CDKAL1*) genotypes, Japan, 2003. Results were adjusted for age, height, and current smoking and alcohol drinking status. The regression lines are indicated in each section: A) TT + CT genotype group (*P* for slope = 0.012); B) CC genotype group (*P* for slope = 0.037); C) both genotype groups (solid line, CC; dotted line, TT + CT). The *P* value for interaction was less than 0.001.

fasting plasma glucose. In this regard, notably, normal HbA1c is associated with markers of inflammation in patients with coronary artery disease (31).

Our results, obtained from a cohort of male workers, corroborate previous reports in which *CDKAL1* genotype was associated with altered insulin responsiveness (10, 14, 15) or the first phase of insulin secretion in normal subjects (32). Moreover, we showed that the *CDKAL1* variant rs9465871 affects HbA1c levels in a manner dependent on increased energy intake, implying that the effect of rs9465871 on glycemic control is influenced by nutritional factors. The association of the *CDKAL1* variant with MetS poses an intriguing question regarding the mechanism of the development and progression of the disease. To the best of our knowledge, this is the first study to have found an interaction effect of the type 2 diabetes genetic marker *CDKAL1* and a lifestyle-related factor, specifically energy intake, on MetS in a healthy Japanese population.

MetS is comprised of 4 typical components: abdominal obesity, hypertension, dyslipidemia, and impaired fasting glucose concentration. Insulin resistance is thought to play a primary role in the pathophysiology of MetS; in the natural course of the disease, insulin resistance is initially counterbalanced by a compensatory increase in insulin secretion to maintain normal glucose tolerance. However, the increase in insulin secretion is eventually unable to offset the severe degree of insulin resistance, and overt type 2 diabetes develops. Our results suggest that β-cell dysfunction might be involved from the early stages of MetS, and it is tempting to speculate that the dysglycemic component of MetS might already be influenced by impaired insulin secretion. We conclude that *CDKAL1*, which is known to play a role in insulin secretion and type 2 diabetes, interacts with energy intake and confers a risk for the dysglycemic phenotype of MetS.

Our study had the following limitations. First, dietary energy intake was self-reported, derived from answers to a validated semiquantitative food frequency questionnaire, which might have introduced measurement bias. Second, the study sample size within this cohort was not large enough to detect a gene-nutrient interaction effect, because the statistical power was low. We speculate that the subjects' unique ethnicity may have been the reason why we detected an interaction. In addition, in a previous study, Jakes et al. (33) reported that energy intake was related to

Downloaded from aje.oxfordjournals.org at Keio University (PULC Consortium) on November 24, 2010

body size, which is correlated with the energy expenditure of physical activity. In our study, we adjusted for body size as a confounding variable; however, there may have been other residual confounding factors not accounted for in our analyses.

The overlap of this genetic risk factor with impaired insulin secretion in patients with type 2 diabetes and MetS suggests a commonality in their etiology. This issue needs to be considered by taking into account ethnic differences, because β-cell function has been shown to be lower in Japanese-American and Chinese-American populations than in African-American and non-Hispanic white populations (34).

Furthermore, Moore et al. (35) reported on the effect of the diabetes gene on lifestyle interventions among nondiabetic high-risk participants in the Diabetes Prevention Program and found no evidence of interactions between *CDKAL1* and lifestyle (or metformin). Thus, the *CDKAL1* polymorphism may potentially play a role in the initial phase of dysglycemia. Our findings suggest that *CDKAL1* may not only be a good genetic marker for the detection of MetS, even in a healthy population, but also may provide descriptive information about lifestyle modification in the prevention of MetS. However, additional studies are warranted for further exploration of the interaction effect, as well as to determine when and how insulin secretion affects the pathogenesis of MetS.

ACKNOWLEDGMENTS

Author affiliations: Department of Neurology, School of Medicine, Keio University, Tokyo, Japan (Koichi Miyaki, Htay Lwin, Yutaka Tomita, Haruhiko Hoshino, Norihiro Suzuki); and Department of Molecular Epidemiology, Medical Research Institute, Tokyo Medical and Dental University, Tokyo, Japan (Koichi Miyaki, Than Oo, Yixuan Song, Htay Lwin, Masaaki Muramatsu).

This study was supported by the Japanese Ministry of Education, Science, Sports, and Culture (Grant-in-Aid for Scientific Research 19590581).

Conflict of interest: none declared.

REFERENCES

1. Eckel RH, Grundy SM, Zimmet PZ. The metabolic syndrome. *Lancet*. 2005;365(9468):1415–1428.
2. Ford ES, Giles WH, Dietz WH. Prevalence of the metabolic syndrome among US adults: findings from the Third National Health and Nutrition Examination Survey. *JAMA*. 2002; 287(3):356–359.
3. Miyatake N, Kawasaki Y, Nishikawa H, et al. Prevalence of metabolic syndrome in Okayama prefecture, Japan. *Intern Med*. 2006;45(2):107–108.
4. Grundy SM, Brewer HB Jr, Cleeman JI, et al. Definition of metabolic syndrome: report of the National Heart, Lung, and Blood Institute/American Heart Association conference on scientific issues related to definition. *Circulation*. 2004;109(3): 433–438.
5. Moller DE, Kaufman KD. Metabolic syndrome: a clinical and molecular perspective. *Annu Rev Med*. 2005;56:45–62.
6. Roche HM, Phillips C, Gibney MJ. The metabolic syndrome: the crossroads of diet and genetics. *Proc Nutr Soc*. 2005;64(3): 371–377.
7. Song Y, Miyaki K, Araki J, et al. The interaction between the interleukin 6 receptor gene genotype and dietary energy intake on abdominal obesity in Japanese men. *Metabolism*. 2007; 56(7):925–930.
8. Zhang L, Miyaki K, Nakayama T, et al. Cell death-inducing DNA fragmentation factor alpha-like effector A (CIDEA) gene V115F (G→T) polymorphism is associated with phenotypes of metabolic syndrome in Japanese men. *Metabolism*. 2008;57(4):502–505.
9. Wellcome Trust Case-Control Consortium. Genome-wide association study of 14,000 cases of seven common diseases and 3,000 shared controls. *Nature*. 2007;447(7145):661–678.
10. Steinthorsdottir V, Thorleifsson G, Reynisdottir I, et al. A variant in CDKAL1 influences insulin response and risk of type 2 diabetes. *Nat Genet*. 2007;39(6):770–775.
11. Zeggini E, Weedon MN, Lindgren CM, et al. Replication of genome-wide association signals in UK samples reveals risk loci for type 2 diabetes. *Science*. 2007;316(5829): 1336–1341.
12. Omori S, Tanaka Y, Takahashi A, et al. Association of CDKAL1, IGF2BP2, CDKN2A/B, HHEX, SLC30A8, and KCNJ11 with susceptibility to type 2 diabetes in a Japanese population. *Diabetes*. 2008;57(3):791–795.
13. Takeuchi F, Serizawa M, Yamamoto K, et al. Confirmation of multiple risk loci and genetic impacts by a genome-wide association study of type 2 diabetes in the Japanese population. *Diabetes*. 2009;58(7):1690–1699.
14. Palmer ND, Goodarzi MO, Langefeld CD, et al. Quantitative trait analysis of type 2 diabetes susceptibility loci identified from whole genome association studies in the Insulin Resistance Atherosclerosis Family Study. *Diabetes*. 2008;57(4): 1093–1100.
15. Stancáková A, Pihlajamäki J, Kuusisto J, et al. Single-nucleotide polymorphism rs7754840 of CDKAL1 is associated with impaired insulin secretion in nondiabetic offspring of type 2 diabetic subjects and in a large sample of men with normal glucose tolerance. EUGENE2 Consortium. *J Clin Endocrinol Metab*. 2008;93(5):1924–1930.
16. Ng MC, Park KS, Oh B, et al. Implication of genetic variants near TCF7L2, SLC30A8, HHEX, CDKAL1, CDKN2A/B, IGF2BP2, and FTO in type 2 diabetes and obesity in 6,719 Asians. *Diabetes*. 2008;57(8):2226–2233.
17. Kim WY, Kim JE, Choi YJ, et al. Nutritional risk and metabolic syndrome in Korean type 2 diabetes mellitus. *Asia Pac J Clin Nutr*. 2008;17(suppl 1):47–51.
18. Kim HS, Park SY, Grandinetti A, et al. Major dietary patterns, ethnicity, and prevalence of type 2 diabetes in rural Hawaii. *Nutrition*. 2008;24(11-12):1065–1072.
19. Wei FY, Nagashima K, Ohshima T, et al. Cdk5-dependent regulation of glucose-stimulated insulin secretion [letter]. *Nat Med*. 2005;11(10):1104–1108.
20. Ubeda M, Rukstalis JM, Habener JF. Inhibition of cyclin-dependent kinase 5 activity protects pancreatic beta cells from glucotoxicity. *J Biol Chem*. 2006;281(39): 28858–28864.
21. Arai H, Yamamoto A, Matsuzawa Y, et al. Prevalence of metabolic syndrome in the general Japanese population in 2000. *J Atheroscler Thromb*. 2006;13(4):202–208.

Downloaded from aje.oxfordjournals.org at Keio University (PULC Consortium) on November 24, 2010

22. Takahashi K, Yoshimura Y, Kaimoto T, et al. Validation of a food frequency questionnaire based on food groups for estimating individual nutrient intake [in Japanese]. *Jpn J Nutr.* 2001;59(5):221–232.
23. Miyaki K, Sutani S, Kikuchi H, et al. Increased risk of obesity resulting from the interaction between high energy intake and the Trp64Arg polymorphism of the β3-adrenergic receptor gene in healthy Japanese men. *J Epidemiol.* 2005;15(6): 203–210.
24. Wu Y, Li H, Loos RJ, et al. Common variants in CDKAL1, CDKN2A/B, IGF2BP2, SLC30A8, and HHEX/IDE genes are associated with type 2 diabetes and impaired fasting glucose in a Chinese Han population. *Diabetes.* 2008;57(10):2834–2842.
25. Bunn HF. Evaluation of glycosylated hemoglobin diabetic patients. *Diabetes.* 1981;30(7):613–617.
26. Larsen ML, Hørder M, Mogensen EF. Effect of long-term monitoring of glycosylated hemoglobin levels in insulin-dependent diabetes mellitus. *N Engl J Med.* 1990;323(15): 1021–1025.
27. Rohlfing CL, Little RR, Wiedmeyer HM, et al. Use of GHb (HbA1c) in screening for undiagnosed diabetes in the U.S. population. *Diabetes Care.* 2000;23(2):187–191.
28. Droumaguet C, Balkau B, Simon D, et al. Use of HbA_{1c} in predicting progression to diabetes in French men and women: Data from an Epidemiological Study on the Insulin Resistance Syndrome (DESIR). *Diabetes Care.* 2006;29(7): 1619–1625.
29. Sung KC, Rhee EJ. Glycated haemoglobin as a predictor for metabolic syndrome in non-diabetic Korean adults. *Diabet Med.* 2007;24(8):848–854.
30. Masuzoe Y. Notification on the criteria for health checkup and health guidance [in Japanese]. Tokyo, Japan: Ministry of Health, Labour and Welfare; 2008. (http://www.mhlw.go.jp/bunya/shakaihosho/iryouseido01/dl/info03i-2.pdf). (Accessed May 1, 2009).
31. Gustavsson CG, Agardh CD. Markers of inflammation in patients with coronary artery disease are also associated with glycosylated haemoglobin A1c within the normal range. Eur Heart J. 2004;25(23):2120–2124.
32. Groenewoud MJ, Dekker JM, Fritsche A, et al. Variants of CDKAL1 and IGF2BP2 affect first-phase insulin secretion during hyperglycaemic clamps. *Diabetologia.* 2008;51(9): 1659–1663.
33. Jakes RW, Day NE, Luben R, et al. Adjusting for energy intake—what measure to use in nutritional epidemiological studies? *Int J Epidemiol.* 2004;33(6):1382–1386.
34. Torréns JI, Skurnick J, Davidow AL, et al. Ethnic differences in insulin sensitivity and beta-cell function in premenopausal or early perimenopausal women without diabetes: the Study of Women's Health Across the Nation (SWAN). *Diabetes Care.* 2004;27(2):354–361.
35. Moore AF, Jablonski KA, McAteer JB, et al. Extension of type 2 diabetes genome-wide association scan results in the Diabetes Prevention Program. *Diabetes.* 2008;57(9):2503–2510.

Downloaded from aje.oxfordjournals.org at Keio University (PULC Consortium) on November 24, 2010

Provided for non-commercial research and education use.
Not for reproduction, distribution or commercial use.

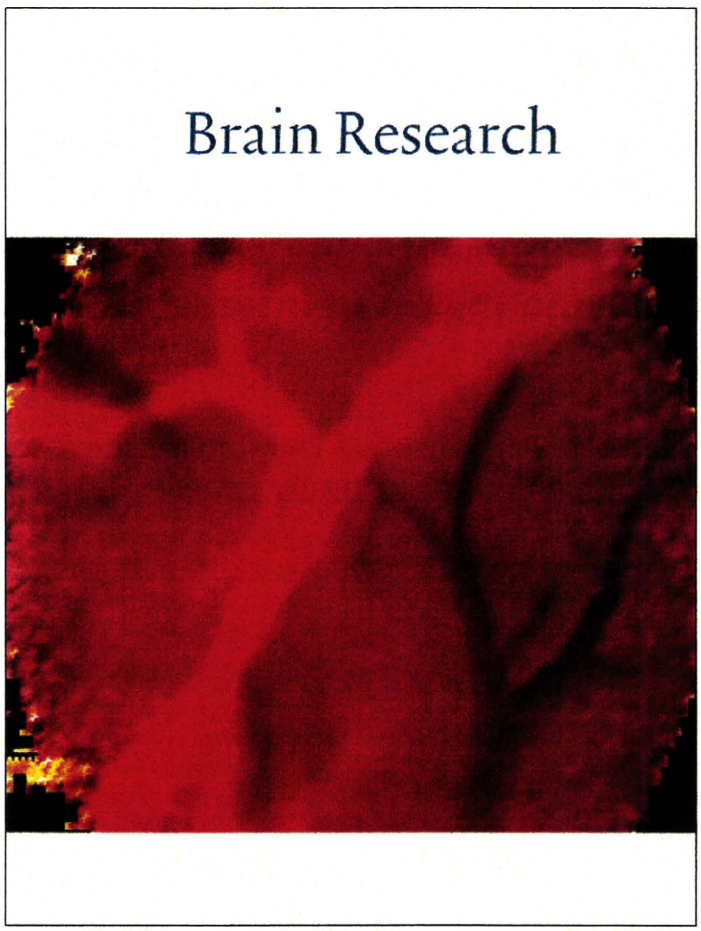

This article appeared in a journal published by Elsevier. The attached copy is furnished to the author for internal non-commercial research and education use, including for instruction at the authors institution and sharing with colleagues.

Other uses, including reproduction and distribution, or selling or licensing copies, or posting to personal, institutional or third party websites are prohibited.

In most cases authors are permitted to post their version of the article (e.g. in Word or Tex form) to their personal website or institutional repository. Authors requiring further information regarding Elsevier's archiving and manuscript policies are encouraged to visit:

http://www.elsevier.com/copyright

BRAIN RESEARCH 1372 (2011) 59–69

available at www.sciencedirect.com

ScienceDirect

www.elsevier.com/locate/brainres

BRAIN RESEARCH

Research Report

Long-term, repeated measurements of mouse cortical microflow at the same region of interest with high spatial resolution

Yutaka Tomita[a,b,c,*], *Elisabeth Pinard*[a], *Alexy Tran-Dinh*[a], *Istvan Schiszler*[b], *Nathalie Kubis*[a], *Minoru Tomita*[b], *Norihiro Suzuki*[b], *Jacques Seylaz*[a]

[a]*Cardiovascular Research Center Lariboisière, INSERM U 689, Université Paris 7, Paris, France*
[b]*Department of Neurology, Keio University School of Medicine, Shinanomachi, Shinjuku-ku, Tokyo, Japan*
[c]*Tomita Hospital, Motojuku-cho, Okazaki, Aichi, Japan*

ARTICLE INFO

Article history:
Accepted 5 November 2010
Available online 25 November 2010

Keywords:
2-D flow map
Confocal microscopy
Focal cerebral ischemia
Mouse
Cerebral blood flow
Optical imaging

ABSTRACT

A method for long-term, repeated, semi-quantitative measurements of cerebral microflow at the same region of interest (ROI) with high spatial resolution was developed and applied to mice subjected to focal arterial occlusion. A closed cranial window was chronically implanted over the left parieto-occipital cortex. The anesthetized mouse was placed several times, e.g., weekly, under a dynamic confocal microscope, and Rhodamine B-isothiocyanate-dextran was each time intravenously injected as a bolus, while microflow images were video recorded. Left and right tail veins were sequentially catheterized in a mouse three times at maximum over a 1.5 months' observation period. Smearing of the input function resulting from the use of intravenous injection was shown to be sufficiently small. The distal middle cerebral artery (MCA) was thermocoagulated through the cranial window in six mice, and five sham-operated mice were studied in parallel. Dye injection and video recording were conducted four times in this series, i.e., before and at 10 min, 7 and 30 days after sham operation or MCA occlusion. Pixelar microflow values (1/MTT) in a matrix of approximately 50×50 pixels were displayed on a two-dimensional (2-D) map, and the frequency distribution of the flow values was also calculated. No significant changes in microflow values over time were detected in sham-operated mice, while the time course of flow changes in the ischemic penumbral area in operated mice was similar to those reported in the literature. This method provides a powerful tool to investigate long-term changes in mouse cortical microflow under physiological and pathological conditions.

© 2010 Elsevier B.V. All rights reserved.

1. Introduction

The heterogeneity of brain tissue and vascularization makes difficult to follow the spatial and temporal evolution of cerebral blood flow (CBF). Presently, CBF spatial heterogeneity is best evaluated using autoradiographic techniques, but this can be done only at a single time point, because the animal must be sacrificed. The microsphere method offers the

* *Corresponding author*. Department of Neurology, Keio University School of Medicine, Shinanomachi, Shinjuku-ku, Tokyo, Japan. Fax: +81 3 3353 1272.
E-mail address: yutakacnrs@aol.com (Y. Tomita).

0006-8993/$ – see front matter © 2010 Elsevier B.V. All rights reserved.
doi:10.1016/j.brainres.2010.11.014